Graphical Abstract



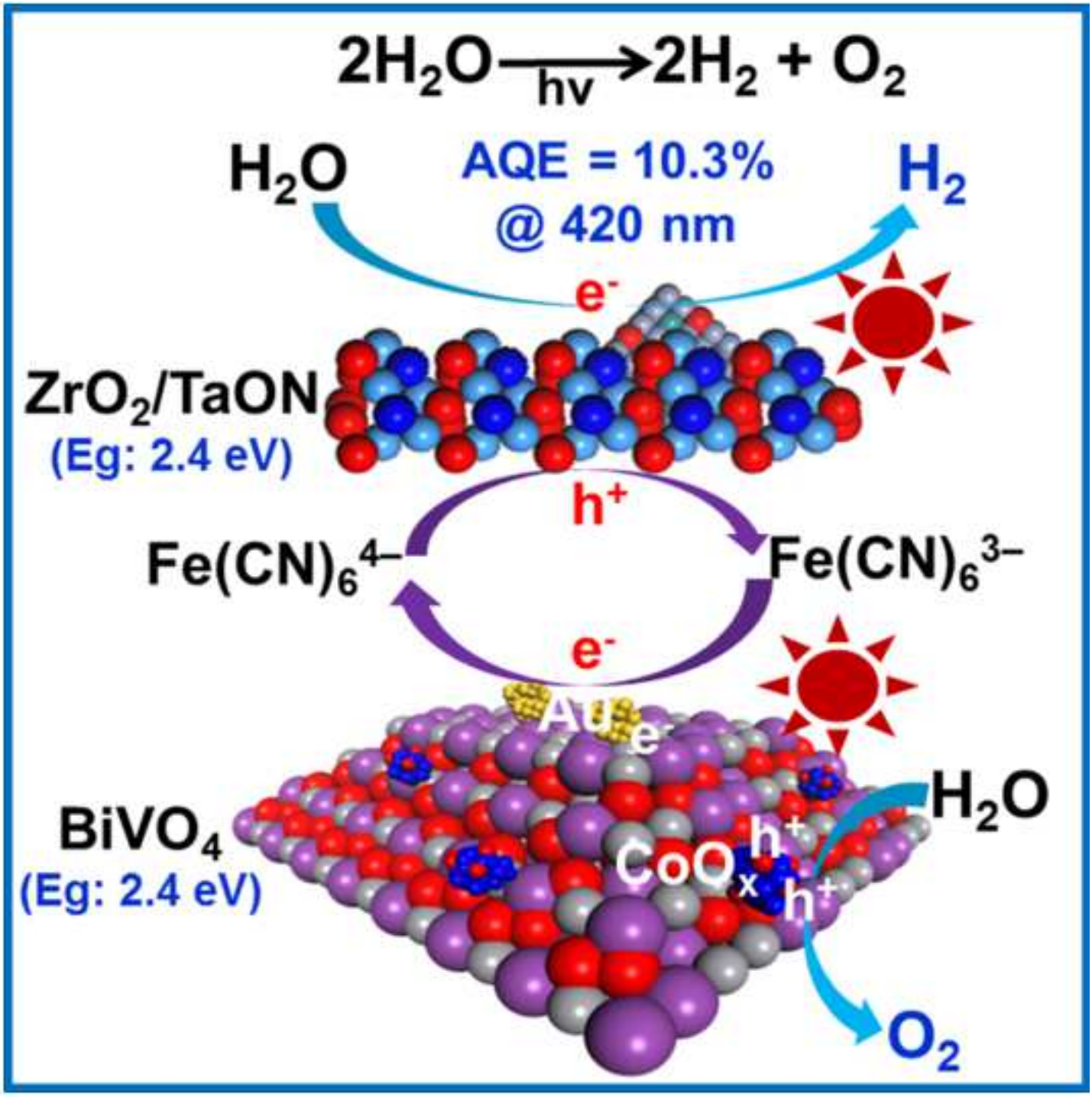

Joule

CellPress

Article

# Redox-based Visible-light-driven Z-scheme Overall Water Splitting with Apparent Quantum Efficiency Exceeding 10%

Yu Qi,[1] Yue Zhao,[1,2] Yuying Gao,[1,2] Deng Li,[1,2] Zhen Li,[1,2] Fuxiang Zhang,[1,3]* and Can Li[1,]**

[1]State Key Laboratory of Catalysis, *i*ChEM, Dalian Institute of Chemical Physics, Chinese Academy of Sciences, Dalian National Laboratory for Clean Energy, Dalian, 116023, China

[2]University of Chinese Academy of Sciences, Beijing, 100049, China

[3]Lead Contact

*Correspondence: fxzhang@dicp.ac.cn

**Correspondence: canli@dicp.ac.cn

## SUMMARY

**To mimic natural photosynthesis, particulate-based Z-scheme overall water splitting (ZOWS) free of external bias is intriguing for hydrogen production, but it commonly confronts low efficiency with huge challenge of charge transfer and separation. Here we report an assembly of unprecedentedly efficient ZOWS system with apparent quantum efficiency (AQE) of 10.3% at 420 nm using $[Fe(CN)_6]^{3-}$/$[Fe(CN)_6]^{4-}$ as redox mediator. The breakthrough of AQE is mainly ascribed to effective cocatalyst strategy that significantly promotes charge transfer and surface catalysis. Meanwhile, the metallic Au cocatalyst is first revealed to favor electron transfer from $BiVO_4$ to $[Fe(CN)_6]^{3-}$ shuttle ions, and site-selective deposition of Au and $CoO_x$ dual cocatalysts on the corresponding electrons-rich {010} and holes-rich {110} facets of $BiVO_4$ is crucial for promotion of water oxidation. This work highlights the importance of cocatalyst strategy as well as site-selective deposition in accelerating charge separation and surface catalysis of artificial photocatalyst for enhanced solar-to-chemical energy conversion.**

## INTRODUCTION

Particulate-based solar water splitting is a promising and economically feasible technology to convert solar energy considering its simplicity and easy scalability.[1-4] To date, two kinds of systems have been developed for this purpose: one is called as one-step photo-excited system, the other is denoted as two-step photo-excited system (also called Z-scheme).[1,5] Regardless of one or two step process, the

construction of overall water splitting (OWS) systems has always confronted huge challenges from both thermodynamic and kinetics aspects because it inevitably involves the four-electron transferred water oxidation uphill reaction.[6-8] Moreover, the powder photocatalysts have to face the challenge of charge separation due to the shortage of external bias. Consequently, the number of OWS systems, especially for visible light driven ones, is still limited, and most reported AQE under visible light irradiation is low.[5,9-13]

Compared to the one-step system, the component of Z-scheme overall water splitting (ZOWS) system is relatively complicated, which is normally composed of $H_2$-evolving photocatalyst (HEP), $O_2$-evolving photocatalyst (OEP) and charge transfer mediator between HEP and OEP (normally employed as shuttle ions or solid conductor).[14-20] The assembly of ZOWS system does not similarly demand the photocatalysts (both HEP and OEP) to simultaneously satisfy water reduction and oxidation as the one-step system. In this case, broader material candidates can be considered and used for ZOWS system. As far as fabrication of solid state ZOWS is concerned, the main challenges lie in the interface charge transfer among HEP, OEP and solid conductor, and inhabitation of short-circuit current among them. Recently, Domen et al., developed photocatalyst sheets-based solid-state ZOWS systems for promoted charge separation as well as significantly enhanced efficiency of ZOWS, but the preparative processes of photocatalyst sheets are relatively complicated leading to greatly enhanced cost.[21-22] Comparatively, the assembly of ZOWS system using shuttle ions and suspended powder photocatalysts has inspired much more interest in the field of ZOWS due to its advantages such as simple technology, cheapness and easy for scale application. However, the disadvantages for the assembly of ZOWS system using shuttle ion as electron transfer mediator are to confront the additional electron transfer between HEP and OEP, and to overcome the competing reactions of shuttle ions with water reduction and oxidation.[23] Accordingly, the choice of shuttle ions, HEP and OEP as well as surface modification such as loading of suitable cocatalyst should be extremely important for assembly of efficient ZOWS system.

To date, some redox shuttle ions have been developed for the construction of ZOWS system [24-31] among which $IO_3^-/I^-$ and $Fe^{3+}/Fe^{2+}$ have been widely investigated. Recently, we have given the first demonstration that $[Fe(CN)_6]^{3-}/[Fe(CN)_6]^{4-}$ redox mediator can be used to fabricate an effective ZOWS system using PSII and Rh-doped $SrTiO_3$ as the OEP and HEP, respectively.[25] Compared to the widely used $IO_3^-/I^-$ or $Fe^{3+}/Fe^{2+}$ shuttle ions, the $[Fe(CN)_6]^{3-}/[Fe(CN)_6]^{4-}$ shuttle ions is demonstrated to exhibit much lower redox potential ($E^\theta$ = 0.357 V vs. NHE), more favorable for storage of solar energy. Furthermore, the $[Fe(CN)_6]^{3-}/[Fe(CN)_6]^{4-}$ shuttle ions can work at much milder pH environment with respect to the $Fe^{3+}/Fe^{2+}$ mediator ($Fe^{3+}/Fe^{2+}$: 2~3; $[Fe(CN)_6]^{3-}/[Fe(CN)_6]^{4-}$: 6~7), and which can be cycled by

accepting/donating one electron instead of multiple electrons like the $IO_3^-/I^-$ ions (6 electrons). Accordingly, the above advantages of $[Fe(CN)_6]^{3-}/[Fe(CN)_6]^{4-}$ redox mediator render it to be a promising candidate for construction of ZOWS system.

$BiVO_4$ (Eg: 2.4 eV)[13,32,33] and $ZrO_2$ modified TaON (Eg: 2.4 eV)[12, 34, 35] have been widely employed as the OEP and HEP for construction of ZOWS in consideration of their suitable band gap, good visible light absorption and photochemical stability. For example, Domen et al., reported the effective ZOWS using $ZrO_2$/TaON as the HEP and $WO_3$ as the OEP, together with $IO_3^-/I^-$ as the redox, achieving 6.3% of AQE at 420 nm[12]. Kudo et al., promoted the efficiency of $SrTiO_3$:Rh-$Fe^{2+/3+}$-$BiVO_4$ system by synthesizing highly active rhodium-doped $SrTiO_3$[13]. Recently we have updated the AQE of redox-based ZOWS to be 6.8% at 420 nm based on the synthesis of TaON-based heterostructure as the HEP.[11] Compared with the water reduction, the water oxidation is normally more challenging for OWS, so continuous efforts are still required to improve the ability of the OEP for enhanced AQE. Towards this goal, the basic concerns should be given for the bulk and surface structure of the OEP to promote the bulk charge separation and surface electron transfer of the OEP to the shuttle ions. Loading of cocatalyst has been demonstrated effective to accelerate the electron transfer.[32,35,36] In addition, we have recently demonstrated the spatial charge separation between the {010} and {110} facets of $BiVO_4$,[37] based on which significantly enhanced oxidation of water or organics can be achieved by loading of dual cocatalysts.[38] Encouraged by these results, it is highly desirable to employ the $BiVO_4$ with facets exposed as the OEP for assembly of efficient ZOWS with $[Fe(CN)_6]^{3-}/[Fe(CN)_6]^{4-}$ as redox mediator.

Here we will introduce the assembly of a highly efficient ZOWS system by using $[Fe(CN)_6]^{3-}/[Fe(CN)_6]^{4-}$ as redox mediator, and employing the facets-controlled $BiVO_4$ and $ZrO_2$ modified TaON (denotes as $ZrO_2$/TaON) as the OEP and HEP, respectively. The working mechanism of ZOWS is illustrated in Scheme 1, as similar to our previous illustration.[23] The optimized AQE can reach as high as 10.3% at 420 nm, which mainly results from significantly enhanced $O_2$ evolution rate on the OEP, as caused by the synergistic promotion effect of site-selective deposition of Au and $CoO_x$ dual cocatalysts on the different facets of $BiVO_4$ for charge separation. The metallic Au photodeposited on the {010} facet of $BiVO_4$ is first demonstrated to better favor the electron transfer from the conduction band of $BiVO_4$ to the $[Fe(CN)_6]^{3-}$ ions compared to other typical metals.

## RESULTS

### Assembly of ZOWS System

Both the OEP and HEP were synthesized by referring to previous works,[39,40] and the detailed experimental procedures are given in experimental procedures. Their single phase of diffraction structure and feature of wide visible light absorption can be revealed by their powder X-ray diffraction and UV-vis DRS (Figure S1). Additionally, their typical morphologies are analyzed by FESEM images and given in Figure S2, based on which the $BiVO_4$ with {010} and {110} facets exposed and $ZrO_2$/TaON with porous feature can be similarly observed as before.[39,40] Figure 1A exhibits the site-selective deposition of Au and $CoO_x$ dual cocatalysts on the corresponding electron-rich {010} and hole-rich {110} facet of $BiVO_4$. The deposited gold and cobalt species were analyzed to exist as metallic Au and cobalt oxide (denotes as $CoO_x$) by XPS measurement[38] (Figure S3 and S4) and HRTEM (Figure 1B and C). The deposited $Rh_yCr_{2-y}O_3$ cocatalyst on the surface of $ZrO_2$/TaON was also analyzed and confirmed by XPS spectra (Figure S5 and S6)[41] and TEM image (Figure S7).

Construction of ZOWS system is demonstrated to be greatly affected by the balance of $H_2$-evolving and $O_2$-evolving rate, which are related to the amount of HEP and OEP, concentration of shuttle ions (see Table S1). Based on our optimization, we can achieve the optimal efficiency of ZOWS by employing 50 mg Au/$CoO_x$-$BiVO_4$, 50 mg $Rh_yCr_{2-y}O_3$-$ZrO_2$/TaON and 10 mM $K_4[Fe(CN)_6]$ as the initial shuttle ions. Figure 2A gives its typical time course of ZOWS, in which the molar ratio of $H_2$ and $O_2$ evolved is kept at 2:1 at the experimental region. The initial rates of $H_2$ and $O_2$ evolution are 130 and 65 μmol/h, respectively. No obvious deactivation is observed for the multiple-cycle time course curves on the optimal ZOWS system in the experimental region (see Figure S8), demonstrating its good photostability. Figure 2B shows the dependence curve of AQE as a function of irradiation wavelength and UV-Vis spectra of HEP and OEP, in which the good accordance of activities with the trend of diffuse reflectance spectra of the OEP and HEP indicates that the ZOWS system is driven by visible light. The optimal AQE of 10.3% is observed under the irradiation of 420 ± 10 nm, which is much higher than our previous reported AQE value (6.8% at 420 nm).[11] To our knowledge, this should be the first ZOWS system using shuttle redoxs as the electron mediator with AQE value exceeding 10% under visible light irradiation. Moreover, the ZOWS can be achieved under the irradiation of 500 ± 10 nm (AQE: 1.9%), demonstrating the wide visible light utilization. The activity was also evaluated under the irradiation of AM 1.5G with the irradiation area of 4 $cm^2$ at 298 K, and the rates of $H_2$ and $O_2$ evolution are about 30 and 15 μmol/h, separately. Based on this, the solar-to-hydrogen (STH) energy conversion efficiency of this system can be calculated to be 0.5%.

### Effect of Cocatalysts on Electron Transfer and Assembly of ZOWS System

To get insight into the successful construction of ZOWS system and its high efficiency, the exchange and transfer ability of electrons between photocatalysts and shuttle ions were thus analyzed and discussed. First of all, the transfer ability of

photogenerated electrons in the conduction band of $BiVO_4$ to the shuttle $[Fe(CN)_6]^{3-}$ ions (i.e. the $O_2$-evolving side) was evaluated by testing the photocatalytic $O_2$-evolving rate on the $BiVO_4$ with various cocatalyst loaded. As seen in Table 1, the $O_2$ evolution rate on the pristine $BiVO_4$ (entry 1) is pretty low, as is different from previous observation that the surface of $BiVO_4$ itself is highly active for water oxidation when $Ag^+$ or $Fe^{3+}$ ions is employed as the electron acceptor.[13,26,40,42-44] This demonstrates that the $BiVO_4$ itself is not so effective for the transfer of photogenerated electrons from its conduction band to $[Fe(CN)_6]^{3-}$ ions, and loading of cocatalyst is highly desirable. For this purpose, deposition of cocatalyst such as Pd, Ag and Au was thus examined. It should be mentioned that the loading of cocatalysts does not affect the band edge absorption of $BiVO_4$ itself, even though slightly different absorption resulting from the loaded metals are found at much longer wavelength (see Figure S9). The loading of Pd and Ag is demonstrated to make a slight promotion on the $O_2$ evolution rate (entries 2 and 3 in Table 1), while unexpectedly the loading of metallic Au makes a more obvious promotion, indicating its better ability of promoting electron transfer from $BiVO_4$ to $[Fe(CN)_6]^{3-}$ ions (entry 4 in Table 1). Since the $O_2$ evolution rate is highly dependent on the loading of reduction cocatalyst, it is reasonable to deduce that the $O_2$-evolving rate is really determined by the rate of photogenerated electron transfer to $[Fe(CN)_6]^{3-}$ ions. That is to say, here the ability of electron transfer from $BiVO_4$ to $[Fe(CN)_6]^{3-}$ ions is the rate-determining step of water oxidation.

It has been widely proven that the deposited reduction cocatalysts is to promote transfer of electrons from the conduction band of one semiconductor because of their difference of Fermi levels.[45] In this work, all above cocatalysts deposited by photocatalysis are confirmed to mainly exist as metallic state by XPS analysis (Figure S4a, S10 and S11)[37,46] and to be site-selectively located on the {010} facets of $BiVO_4$ by FESEM images (Figure S12). Accordingly, the photogenerated electrons on the {010} facets of $BiVO_4$ are expected to be transferred to the surface of the cocatalysts, so the different $O_2$ evolution rate should be mainly ascribed to their different ability to reduce the $[Fe(CN)_6]^{3-}$ ions leading to distinct electron transfer efficiency. The different reduction abilities of cocatalysts to the $[Fe(CN)_6]^{3-}$ ions can be confirmed by the electrochemical linear sweep voltammetry (LSV) curves given in Figure 3A, where the Au-$BiVO_4$/FTO electrode exhibits the much more negative onset potential and better cathode currents compared to $BiVO_4$/FTO, Pd-$BiVO_4$/FTO, or Ag-$BiVO_4$/FTO electrodes, indicating that the Au loaded on the surface of $BiVO_4$ can better reduce the $K_3[Fe(CN)_6]$ with respect to the Pd or Ag loaded. The functions of cocatalysts can be further revealed by electrochemical impedance spectra (EIS) analysis. An equivalent circuit (inserted into Figure 3B) is used to simulate the electrode and interface, in which $R_s$ is the serial resistance in the circuit and $R_{ct}$ is the charge transfer resistance across the semiconductor/electrolyte interface. As seen in Figure 3B, the samples with loading of Pd, Ag or Au exhibits obviously decreased

charge transfer resistance compared to the pristine $BiVO_4$ sample, among which the Au-$BiVO_4$/FTO electrode shows the smallest charge transfer resistance (values of $R_{ct}$ are listed in Table S2). This indicates that the loading of Au, Pd or Ag can all accelerate surface reduction of $K_3[Fe(CN)_6]$ to $K_4[Fe(CN)_6]$, among which the deposited Au is the most efficient. As an extended discussion, the photocatalytic $O_2$ evolution rate on the Au-$WO_3$, Au-P25 or Au-$SrTiO_3$ sample in the presence of $[Fe(CN)_6]^{3-}$ ions is also found to be much better than that of the corresponding samples without Au cocatalyst (Table S3), revealing that the promotion effect of Au on the electron transfer and exchange between photocatalyst and $[Fe(CN)_6]^{3-}$ ions is of a certain generality.

Besides the deposited Au species itself, the deposition site of Au is also important. As seen in entry 5 of Table 1, the impregnated metallic Au (confirmed by XPS analysis given in Figure S13 and S14)[38] with random dispersion on the surface of $BiVO_4$ (Figure S15) makes a less promotion on the $O_2$ evolution with respect to the sample with Au selectively deposited (entry 4 of Table 1). Interestingly, the promotion effect of electron transfer from the conduction band of $BiVO_4$ to the $[Fe(CN)_6]^{3-}$ ions can be further enlarged by co-loading of dual cocatalysts (Au and $CoO_x$), which are site-selectively deposited on the {010} and {110} facets of $BiVO_4$ (Figure 1a and entry 6, Table 1), respectively. Similarly, the promotion effect is also not obvious when the Au and $CoO_x$ cocatalysts are randomly deposited (see FESEM image, Figure S16) by impregnation method (entry 7, Table 1). These phenomena are very similar to our previous observations,[37] which has been mainly ascribed to the following points: i) the photogenerated electrons and holes can be spatially separated and accumulated on the surface of {010} and {110} facets of $BiVO_4$, respectively; ii) the deposited Au and $CoO_x$ can transfer electrons and holes separately, so the site-selective deposition of Au and $CoO_x$ on the electrons and holes accumulated facets is more favorable for their transfer and promotion of charge separation; iii) the deposition of Au and $CoO_x$ dual cocatalyst makes a synergetic effect on the charge separation as well as $O_2$ evolution. Besides the detection of $O_2$ evolution, another indicator for the effective electron transfer is that the characteristic absorption peak of $K_3[Fe(CN)_6]$ at around 420 nm of UV-Vis spectra (Figure S17) is almost decreased to zero after 1 h irradiation on the Au/$CoO_x$-$BiVO_4$ photocatalyst. What's more, the LSV curves of the reaction solution before and after irradiation were tested to prove the transformation of $K_3[Fe(CN)_6]$ to $K_4[Fe(CN)_6]$. As shown in the Figure S18, only the reduction peak of $K_3[Fe(CN)_6]$ (Figure S18A) and no oxidation peak of $K_4[Fe(CN)_6]$ (Figure S18B) are observed for the reaction before irradiation, While only the oxidation peak of $K_4[Fe(CN)_6]$ (Figure S18B) and no reduction peak of $K_3[Fe(CN)_6]$ (Figure S18A) are observed for the solution after irradiation. This well reveals that the $K_3[Fe(CN)_6]$ has been all reduced into $K_4[Fe(CN)_6]$ during the reaction of $O_2$ evolution.

The different promotion effect of the loaded Au and/or $CoO_x$ cocatalyst on the charge separation of $BiVO_4$ can be confirmed by the results of surface photovoltage (SPV) spectra given in Figure 3C, where loading single Au or $CoO_x$ cocatalyst shows obvious SPV amplitude with respect to the pristine $BiVO_4$, while the sample with both Au and $CoO_x$ modified (Au/$CoO_x$-$BiVO_4$) exhibits the greatest SPV amplitude. It should be pointed out that the SPV values on the Au-modified samples are decreased under the irradiation of above 500 nm compared with the pristine $BiVO_4$ sample, as ascribed to the competition of light absorption caused by Au plasma resonance effect. This also demonstrates that the Au plasmonic effect does not make a positive effect on the charge separation.

The electron transfer ability from the $[Fe(CN)_6]^{4-}$ ions to the valence band of $ZrO_2$/TaON (i.e. the $H_2$-evolving side) was evaluated by the $H_2$ evolution rate. As given in Figure S19, no obvious $H_2$ evolution can be observed for the pristine $ZrO_2$/TaON. However, after loading of cocatalyst $Rh_yCr_{2-y}O_3$, the $H_2$ evolution can be obviously detected. It indicates that the electron transfer from the $[Fe(CN)_6]^{4-}$ ions to the valence band of $ZrO_2$/TaON is feasible, and loading $H_2$-evolving cocatalyst is desirable for the $H_2$ evolution. It should be pointed out that the light absorption of $ZrO_2$/TaON is not remarkably affected after loading of $Rh_yCr_{2-y}O_3$ cocatalyst (Figure S20). The typical time courses of $H_2$ evolution on the $Rh_yCr_{2-y}O_3$-$ZrO_2$/TaON photocatalyst (Figure S19) indicate the $[Fe(CN)_6]^{4-}$ ions added can be completely oxidized into $[Fe(CN)_6]^{3-}$ ions to produce stoichiometric $H_2$ (50 μmol) in 40 mins' irradiation, demonstrating the effectiveness of the electron transfer. The effective electron transfer can be also confirmed by the result of UV-Vis spectra (Figure S21), where the characteristic absorption of $K_4[Fe(CN)_6]$ disappears and the absorption peak intensity of $K_3[Fe(CN)_6]$ at around 420 nm is greatly increased from zero. As similar to the $O_2$-evolving reaction, the LSV measurement further reveals the transformation of $K_4[Fe(CN)_6]$ to $K_3[Fe(CN)_6]$ during the $H_2$-evolving reaction. (Figure S22).

## DISCUSSION

We give the clear illustration that the deposited metallic Au is favorable for reduction of $[Fe(CN)_6]^{3-}$ ions to achieve effective electron transfer, which is one of the crucial steps towards the achievement of ZOWS. Additionally, the site-selective deposition strategy of dual cocatalysts is revealed to efficiently promote charge separation in both bulk of OEP and interface between OEP and $[Fe(CN)_6]^{3-}$ ions. Based on the finding of Au cocatalyst and strategy of dual cocatalysts with site-selective deposition, we fabricate a highly efficient visible-light-driven ZOWS system with optimal AQE of 10.3% at 420 nm and STH of 0.5%. To our knowledge, this should be the first ZOWS system using shuttle redox as the electron mediator with AQE value exceeding 10% under visible light irradiation. As a comparison, representative redox-based visible-light-driven Z-scheme overall water splitting systems which have

been reported are summarized in Table S4. Compared to previous reports, the significantly enhanced AQE of particulate-based ZOWS should be extremely encouraging in the field of solar-to-chemical energy conversion. This work also demonstrates bright future of the $[Fe(CN)_6]^{3-}/[Fe(CN)_6]^{4-}$ redox mediator in constructing effective artificial photosynthesis devices.

## EXPERIMENTAL PROCEDURES

### Synthesis of HEP and OEP.

$ZrO_2$-modified TaON (denotes as $ZrO_2$/TaON, the molar ratio of Zr/Ta is 0.1) sample was used as the HEP, which was synthesized by nitridation of the $ZrO_2/Ta_2O_5$ composite under an ammonia flow (20 mL $min^{-1}$) at 1123 K for 15 h according to the previous work.[39] It is worth noting that the role of $ZrO_2$ modification on TaON has been discussed and ascribed to mainly suppress the formation of surface defect on TaON by inhibiting the tantalum reduction during nitridation under the flow of ammonia at high temperature.[39] As for $BiVO_4$, it was prepared by a hydrothermal procedure.[40] Typically, $NH_4VO_3$ (10 mmol) and $Bi(NO_3)_3$ $5H_2O$ (10 mmol) were dissolved in 60 mL of 2.0 M nitric acid solution, and the pH value of the solution was then adjusted to 0.5 with ammonia solution (25-28 *wt*%) under stirring until formation of a light yellow precipitate. After about 2 h aging, the light yellow precipitate at the bottom of the beaker was transferred to a Teflon-lined stainless steel autoclave with a capacity of 100 mL and hydrothermally treated at 473K for 10 h.

### Deposition of Cocatalysts and Preparation of Electrodes.

For the deposition of cocatalyst on the surface of the OEP, *in-situ* photodeposition method was adopted. Typically, 0.2 g $BiVO_4$ sample was dispersed in deionized water and a calculated amount of metal precursors (0.8 *wt*%) was added. Afterwards the suspension was irradiated under 300 W Xe lamp with the full-spectral irradiation for 2 h. Through filtration, washing and dry, the as-obtained powder was loaded with $CoO_x$ (0.1 *wt*%) by *in-situ* photochemical deposition method in the sodium potassium buffer solution (PBS) (pH = 6.0 50 mM) containing a calculated amount of $CoSO_4$ for 1 h. As for the Au(Imp.)-$BiVO_4$, the conventional impregnation and subsequent hydrogen reduction method was adopted. Typically, 0.2 g $BiVO_4$ sample was immersed in a calculated $HAuCl_4$ (0.8 *wt*%) aqueous solution with ultrasonic agitation for ca. 5 min. After the solution was completely evaporated in a water bath at 353 K, the impregnated powder was collected and reduced at 573 K for 1 h under a flow of 5% $H_2$/Ar (200 mL $min^{-1}$). The preparation of Au/$CoO_x$(Imp.)-$BiVO_4$ is almost the same as the Au(Imp.)-$BiVO_4$ except that the impregnated powder was calcined under the air at 573 K for 1 h.

The deposition of nanoparticle rhodium chromium mixed-oxides (donated as $Rh_yCr_{2-y}O_3$) on the surface of the HEP as the cocatalyst was carried out by photodeposition method. 0.2 g $ZrO_2$/TaON was dispersed in 20 *v*% 150 mL methanol solution. A certain amount of $Na_3RhCl_6$ and $K_2CrO_4$ (1.0 *wt*% Rh and 1.5 *wt*% Cr vs. photocatalyst) were added as the precursors and the deposition was carried out under the full-spectral irradiation of 300 W Xe lamp for 6 h. After the photodeposition, the final product was centrifuged and washed with distilled water, then dried at 353 K for overnight.

As for the $BiVO_4$ photoanode, it was prepared according to the previous work.[47] First, spin-coating the $BiVO_4$ seed on the FTO followed by heat treatment and then the prefabricated $BiVO_4$ seed layer on the FTO substrate was immersed in the reaction solution for hydrothermal treatment. Finally, the hydrothermally reacted substrate was heat treated. The cocatalyst on the $BiVO_4$ photoanode was loaded by the *in-situ* photodeposition method like above.

## ACKNOWLEDGMENTS

This work was financially supported by Natural Science Foundation of China (21633009, 21522306, 21633010), the Basic Research Program of China (973 Program: 2014CB239403) and Dalian Science Foundation for Distinguished Young Scholars. F. Zhang thanks the priority support from the “Hundred Talents Program” of Chinese Academy of Sciences.

## AUTHOR CONTRIBUTIONS

F. Z. and C. L. designed the experiments, Y. Q. performed the main experiments, Y. Z. synthesized the $BiVO_4$, Y. G. conducted the SPV measurement, D. L. synthesized the photoanode and conducted the EIS measurement, F. Z., C. L. and Y. Q. analyzed the data and co-wrote the manuscript. All authors discussed the results.

## DECLARATION OF INTERESTS

The authors declare no competing interests.

## REFERENCES

1. Fabian, D.M., Hu, S., Singh, N., Houle, F.A., Hisatomi, T., Domen, K., Osterloh, F.E. and Ardo, S. (2015). Particle suspension reactors and materials for solar-driven water splitting. Energy Environ. Sci., *8*, 2799–3050.

2. Kudo, A., and Miseki, Y. (2009). Heterogeneous photocatalyst materials for water splitting. Chem. Soc. Rev., *38*, 253–278.
3. Osterloh, F.E., (2013). Inorganic nanostructures for photoelectrochemical and photocatalytic water splitting. Chem. Soc. Rev., *42*, 2294–2320.
4. Zhang, P., Wang, T. and Gong, J. (2018). Current Mechanistic Understanding of Surface Reactions over Water-Splitting Photocatalysts. Chem, *4*, 223-245.
5. Chen, S., Takata, K., and Domen, K. (2018). Particulate photocatalysts for overall water splitting. Nat. Rev. Mater., *2*, 17050.
6. Meyer, T.J.(2008). Catalysis: the art of splitting water. Nature, *451*, 778–779.
7. Yi, Z., Ye, J., Kikugawa, N., Kako, T., Ouyang, S., Stuart-Williams, H., Yang, H., Cao, J., Luo, W., Li, Z., Liu, Y., and Withers, R.L. (2010). An orthophosphate semiconductor with photooxidation properties under visible-light irradiation. Nat. Mater., *9*, 559–564.
8. Duan, L., Bozoglian, F., Mandal, S., Stewart, B., Privalov, T., Liobe, A., and Li, C.S. (2012). A molecular ruthenium catalyst with water-oxidation activity comparable to that of photosystem II. Nat. Chem., *4*, 418–423.
9. Maeda, K., Teramura, K., Lu, D., Takata, T., Saito, N., Inoue, Y., and Domen, K. (2006). Photocatalyst releasing hydrogen from water. Nature, *440*, 295.
10. Goto, Y., Hisatomi, T., Wang, Q., Higashi. T., Ishikiriyama, K., Maeda, T., Sakata, Y., Okunaka, S., Tokudome, H., Katayama, M., Akiyama. S., Nishiyama, H., Inoue Y., Takewaki, T., Setoyama, T., Minegishi, T., Takata, T., Yamada, T., and Domen, K. (2018). A particulate photocatalyst water-splitting panel for large-scale solar hydrogen generation. Joule, *2*, 509–520.
11. Chen, S., Qi, Y., Hisatomi, T., Ding, Q., Asai, T., Li, Z., Ma, S.S.K., Zhang, F., Domen, K., and Li, C. (2015). Efficient visible-light-driven Z-scheme overall water splitting using a $MgTa_2O_{6-x}N_y$/TaON heterostructure photocatalyst for $H_2$ evolution. Angew. Chem. Int. Ed., *54*, 8498–8501.
12. Maeda, K., Higashi, M., Lu, D., Abe, R., and Domen, K. (2010). Efficient nonsacrificial water splitting through two-step photoexcitation by visible light using a modified oxynitride as a hydrogen evolution photocatalyst. J. Am. Chem. Soc., *132*, 5858–5868.
13. Kato, H., Sasaki, Y., Shirakura, N., and Kudo, A. (2013). Synthesis of highly active rhodium-doped $SrTiO_3$ powders in Z-scheme systems for visible-light-driven photocatalytic overall water splitting. J. Mater. Chem. A, *1*, 12327–12333.
14. Bard, A.J. (1979). Photoelectrochemistry and heterogeneous photo-catalysis at semiconductor. J. Photochem., *10*, 59–75.
15. Abe, R. (2011). Development of a new system for photocatalytic water splitting into $H_2$ and $O_2$ under visible light irradiation. Bull. Chem. Soc. Jpn., *84*, 1000–1030.
16. Kudo, A. (2011). Z-scheme photocatalyst systems for water splitting under visible light irradiation. MRS Bull., *36*, 32–38.
17. Maeda, K. (2013). Z-Scheme water splitting using two different semiconductor photocatalysts. ACS Catal., *3*, 1486–1503.
18. Li, H., Tu, W., Zhou, Y., and Zou, Z. (2016). Z-scheme photocatalytic systems for promoting photocatalytic performance: recent progress and future challenges. Adv. Sci. 2016, *3*, 1500389.
19. Zong, X., Lu, G., and Wang, L. (2013). Nanocatalysts for water splitting. Nanocatalysis Synthesis and Applications, 495–559.
20. Wang, L., Zheng, X. S., Chen, L., Xiong Y. J. and Xu, H. X. (2018) Van der Waals Heterostructures Comprised of Ultrathin Polymer. Angew. Chem. Int. Ed., *57*, 3454–3458.
21. Wang, Q., Hisatomi, T., Jia, Q., Tokudome, H., Zhong, M., Wang, C., Pan, Z., Takata, T., Nakabayashi, M., Shibata, N., Li, Y., Sharp, I., Kudo A., Yamada, T., and Domen K., (2016) Scalable water splitting on particulate photocatalyst sheets with a solar-to-hydrogen energy conversion eciency exceeding 1%. Nature Materals, *15*(6) : 611.

22. Wang, Q., Hisatomi, T., Suzuki Y., Pan, Z., Seo, J., Katayama M., Minegishi, T., Nishiyama, H., Takata T., Seki K., Kudo A., Yamada, T., and Domen K. (2017) Particulate photocatalyst sheets based on carbon conductor layer for efficient Z-scheme pure water splitting at ambient pressure. J. Am. Chem. Soc., *139*(4): 1675–1683.
23. Qi, Y., Chen, S., Cui, J., Wang, Z., Zhang, F., and Li, C. (2018). Inhibiting competing reactions of iodate/iodide redox mediators by surface modification of photocatalysts to enable Z-scheme overall water splitting. Appl Catal B: Environ., *224*, 579–585.
24. Abe, R., Shinmei, K., Koumura, N., Hara, K., and Ohtani, B. (2013). Visible-light-induced water splitting based on two-step photoexcitation between Dye-sensitized layered niobate and tungsten oxide photocatalysts in the presence of a triiodide/iodide shuttle redox mediator. J. Am. Chem. Soc., *135*, 16872–16884.
25. Wang, W., Chen, J., Li, C., and Tian, W. (2014). Achieving solar overall water splitting with hybrid photosystems of photosystem II and artificial photocatalysts. Nature Commun., *5*: 4647.
26. Kato, H., Hori, M., Konta, R., Shimodaira, Y., and Kudo, A. (2004). Construction of Z-scheme type heterogeneous photocatalysis systems for water splitting into $H_2$ and $O_2$ under visible light irradiation. Chem. Lett., *33*, 1348–1349.
27. Tsuji, K., Tomita, O., Higashi, M., and Abe, R. (2016). Manganese-substituted polyoxometalate as an effective shuttle redox mediator in Z-scheme water splitting under visible light. ChemSusChem, *9*, 2201–2208.
28. Kato, T., Hakari, Y., Ikeda, S., Jia, Q., Iwase, A., and A. Kudo, (2015). Utilization of metal sulfide material of $(CuGa)_{1-x}Zn_{2x}S_2$ solid solution with visible light response in photocatalytic and photoelectrochemical solar water splitting systems. J. Phys. Chem. Lett., *6*, 1042–1047.
29. Abe, R., Sayama, K., Domen, K., and Arakawa, H. (2001). A new type of water splitting system composed of two different $TiO_2$ photocatalysts (anatase, rutile) and a $IO_3^-/I^-$ shuttle redox mediator. Chem. Phys. Lett., *344*, 339–344.
30. Sasaki, Y., Kato, H., and Kudo, A. (2013). $[Co(bpy)_3]^{3+/2+}$ and $[Co(phen)_3]^{3+/2+}$ electron mediators for overall water splitting under sunlight irradiation using Z-scheme photocatalyst system. J. Am. Chem. Soc, *135*, 5441–5449.
31. Miseki, Y., Fujiyoshi, S., Gunji, T., and Sayama, K. (2017). Photocatalytic Z-scheme water splitting for independent $H_2/O_2$ production via a stepwise operation employing a vanadate redox mediator under visible light. J. Phys. Chem. C, *121*, 9691–9697.
32. Sasaki, Y., Iwase, A., Kato, H., and Kudo, A. (2008). The effect of co-catalyst for Z-scheme photocatalysis systems with an $Fe^{3+}/Fe^{2+}$ electron mediator on overall water splitting under visible light irradiation. J. Catal., *259*, 133–137
33. Kato, H., Sasaki, Y., Iwase, A., and Kudo, A. (2007). Role of iron ion electron mediator on photocatalytic overall water splitting under visible light irradiation using Z-scheme systems. Bull.Chem. Soc. Jpn., *80*, 2457–2464.
34. Tabata, M., Maeda, K., Higashi, M., Lu, D., Takata, K., Abe, R., and Domen, K. (2010). Modified $Ta_3N_5$ powder as a photocatalyst for $O_2$ evolution in a two-step water splitting system with an iodate/iodide shuttle redox mediator under visible light. Langmuir, *26*, 9161–9165.
35. Maeda, K., Abe, R., and Domen, K. (2011). Role and function of ruthenium species as promoters with TaON-based photocatalysts for oxygen evolution in two-step water splitting under visible light. J. Phys Chem. C, *115*, 3057–3064.
36. Ma, S. S. K., Maeda, K., Abe, R., and Domen, K. (2012). Visible-light-driven nonsacrificial water oxidation over tungsten trioxide powder modified with two different cocatalysts. Energy Environ. Sci., *5*, 8390–8397.
37. Li, R., Zhang, F., Wang, D., Yang, J., Li, M., Zhu, J., Zhou, X., and Han, H., and Li, C. (2013). Spatial separation of photogenerated electrons and holes among {010} and {110} crystal facets of $BiVO_4$. Nature Commun., *4*: 1432.

38. Li, R., Han, H., Zhang, F., Wang, D., and Li, C. (2014). Highly efficient photocatalysts constructed by rational assembly of dual-cocatalysts separately on different facets of $BiVO_4$. Energy Environ. Sci., *7*, 1369–1376.
39. Maeda, K., Terashima, H., Kase, K., Higashi, M., Tabata, M., and Domen, K. (2008). Surface modification of TaON with nonoclinic $ZrO_2$ to produce a composite photocatalyst with enhanced hydrogen evolution activity under visible light. Bull. Chem. Soc. Jpn., *81*, 927–937.
40. Zhao, Y., Li, R., Mu, L., and Li, C. (2017). Significance of crystal morphology controlling in semiconductor-based photocatalysis: a Case study on $BiVO_4$ photocatalyst. Cryst. Growth Des., *107*, 2923–2928.
41. Maeda, K., Teramura, K., Masuda, H., Takata, T., Saito, N., Inoue, Y., and Domen, K. (2006). Efficient overall water splitting under visible-light irradiation on $(Ga_{1-x}Zn_x)(N_{1-x}O_x)$ dispersed with Rh-Cr mixed-oxide nanoparticles: effect of reaction conditions on photocatalytic activity. J. Phys. Chem. B, *110*, 13107–13112.
42. Kudo, A., Ueda, K., Kato, H., and Mikami, I. (1998). Photocatalytic $O_{-2}$ evolution under visible light irradiation on $BiVO_4$ in aqueous $AgNO_3$ solution. Catal. Lett., *53*, 229–230.
43. Kudo, A., Omori, K., and Kato, H. (1999). A novel aqueous process for preparation of crystal form-controlled and highly crystalline $BiVO_4$ powder from layered vanadates at room temperature and its photocatalytic and photophysical properties. J. Am. Chem. Soc., *121*, 11459–11467.
44. Yu, J., and Kudo, A. (2006). Effects of structural variation on the photocatalytic performance of hydrothermally synthesized $BiVO_4$. Adv. Funct. Mater., *16*, 2163–2169.
45. Yang, J., Wang, D., Han, H., and Li, C. (2013). Roles of cocatalysts in photocatalysis and photoelectrocatalysis. Acc. Chem. Res., *46*, 1900–1909.
46. Li, Z., Zhang, F., Han, H., Han, J., Zhu, J., Li, M., Zhang, B., Fan, W., Lu, J., and Li, C. (2018). Using Pd as a cocatalyst on GaN–ZnO solid solution for visible-light-driven overall water splitting. Catal. Lett., *148*: 933–939.
47. Kim, C.W., Son, Y.S., Kang, M.J., Kim, D.Y., and Kang, Y.S. (2016). (040)-Crystal facet engineering of $BiVO_4$ plate photoanodes for solar fuel production. Adv. Energy. Mater., *6*, 1501754.

**Scheme 1. A Schematic Description of ZOWS Reaction.**

**Figure 1. The Site-selective Deposition of Au and $CoO_x$ Dual Cocatalysts on $BiVO_4$.**

(A) Representative FESEM image of Au/$CoO_x$-$BiVO_4$ sample, and HRTEM image of Au/$CoO_x$-$BiVO_4$ sample: (B) Au; (C) $CoO_x$.

**Figure 2. The Photocatalytic Performance of ZOWS System.**

(A) Time course of ZOWS on the optimized conditions under visible light irradiation [a]; (B) The dependence curve of apparent quantum efficiency (AQE) as a function of irradiation wavelength and diffuse reflectance spectra of the HEP and OEP [b].

a Reaction conditions: 50 mg OEP (0.8 *wt*% Au; 0.1 *wt*% $CoO_x$), 50 mg HEP (1.0 *wt*% Rh, 1.5 *wt*% Cr), 100 mL 25 mM sodium phosphate buffer solution (PBS pH = 6.0) containing $K_4[Fe(CN)_6]$ (10 mM), 300 W xenon lamp (λ ≥ 420 nm), temperature: 288 K, Pyrex top-irradiation type.

b Reaction conditions: 75 mg OEP (0.8 *wt*% Au; 0.1 *wt*% $CoO_x$), 75 mg HEP (1.0 *wt*% Rh, 1.5 *wt*% Cr), 150 mL 25 mM sodium phosphate buffer solution (PBS pH = 6.0) containing $K_4[Fe(CN)_6]$ (10 mM), 300 W xenon lamp (λ ≥ 420 nm), temperature: 298 K, Pyrex top-irradiation type.

**Table 1. Rates of $O_2$ Evolution on the $BiVO_4$ Loaded With Different Cocatalysts [a]**

| entry | cocatalyst | $O_2$ evolution rate (μmol/h) |
|---|---|---|
| 1 | none | 2.4 |
| 2 | Pd | 3.4 |
| 3 | Ag | 5.2 |
| 4 | Au | 14.0 |
| 5 | Au[b] | 5.0 |
| 6 | $Au/CoO_x$ | 32.0 |
| 7 | $Au/CoO_x$[b] | 10.8 |

[a] Reaction conditions: 20 mg photocatalyst; 20 mL 50 mM sodium phosphate buffer solution (PBS pH = 6.0) containing $K_3[Fe(CN)_6]$ (5 mM); 300 W xenon lamp (λ ≥ 420 nm),0.5 h top-irradiation.

[b] Impregnation method.

**Figure 3. The Functions of Cocatalysts and Promotion of Charge Separation with Dual-Cocatalys**

(A) Comparison of electrochemical linear sweep voltammetry (LSV) curves of typical samples in the PBS solution (pH=6.0 100 mM) containing 5 mM $K_3[Fe(CN)_6]$; (B) Comparison of electrochemical impedance spectra (EIS) of typical samples; (C) Comparison of surface photovoltage (SPV) spectra of typical samples (irradiated from 400 nm to 600 nm, with a 500 W xenon lamp).

Joule CellPress

# Figures

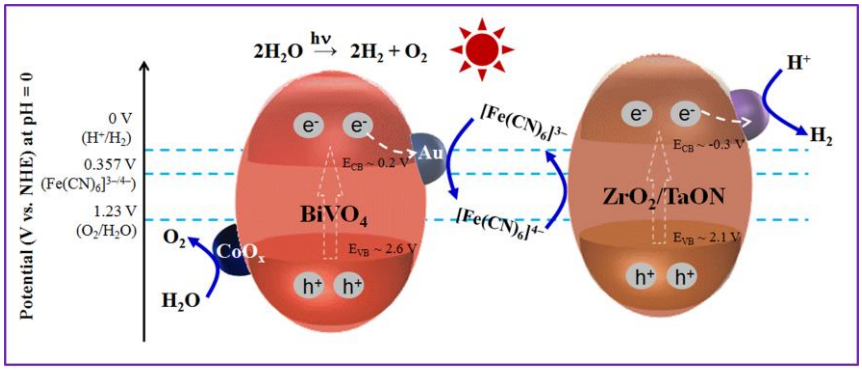


**Scheme 1. A Schematic Description of ZOWS Reaction.**

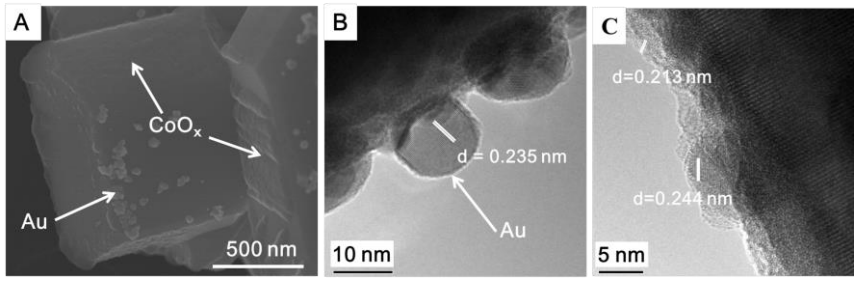


**Figure 1. The Site-selective Deposition of Au and $CoO_x$ Dual Cocatalysts on $BiVO_4$.**

(A) Representative FESEM image of Au/$CoO_x$-$BiVO_4$ sample, and HRTEM image of Au/$CoO_x$-$BiVO_4$ sample: (B) Au; (C) $CoO_x$.

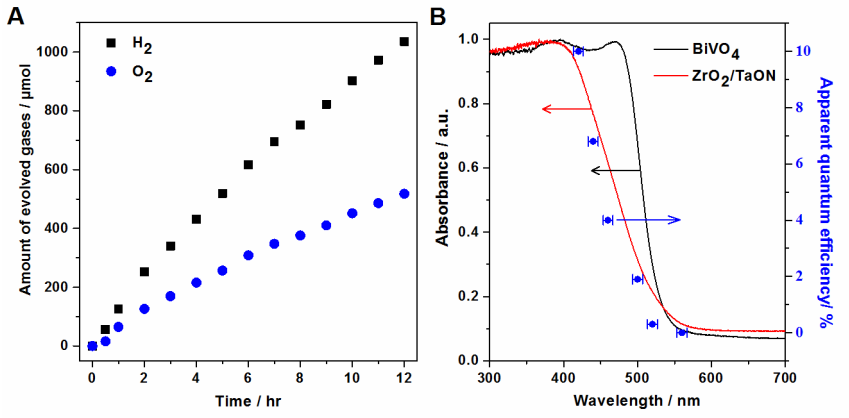


**Figure 2. The Photocatalytic Performance of ZOWS System.**

(A) Time course of ZOWS on the optimized conditions under visible light irradiation [a]; (B) The dependence curve of apparent quantum efficiency (AQE) as a function of irradiation wavelength and diffuse reflectance spectra of the HEP and OEP [b].

a Reaction conditions: 50 mg OEP (0.8 *wt*% Au; 0.1 *wt*% $CoO_x$), 50 mg HEP (1.0 *wt*% Rh, 1.5 *wt*% Cr), 100 mL 25 mM sodium phosphate buffer solution (PBS pH = 6.0) containing $K_4[Fe(CN)_6]$ (10 mM), 300 W xenon lamp (λ ≥ 420 nm), temperature: 288 K, Pyrex top-irradiation type.

b Reaction conditions: 75 mg OEP (0.8 *wt*% Au; 0.1 *wt*% $CoO_x$), 75 mg HEP (1.0 *wt*% Rh, 1.5 *wt*% Cr), 150 mL 25 mM sodium phosphate buffer solution (PBS pH = 6.0) containing $K_4[Fe(CN)_6]$ (10 mM), 300 W xenon lamp (λ ≥ 420 nm), temperature: 298 K, Pyrex top-irradiation type.

**Table 1. Rates of $O_2$ Evolution on the $BiVO_4$ Loaded With Different Cocatalysts [a]**

| entry | cocatalyst | $O_2$ evolution rate (μmol/h) |
|---|---|---|
| 1 | none | 2.4 |
| 2 | Pd | 3.4 |
| 3 | Ag | 5.2 |
| 4 | Au | 14.0 |
| 5 | Au[b] | 5.0 |
| 6 | $Au/CoO_x$ | 32.0 |
| 7 | $Au/CoO_x$[b] | 10.8 |

[a] Reaction conditions: 20 mg photocatalyst; 20 mL 50 mM sodium phosphate buffer solution (PBS pH = 6.0) containing $K_3[Fe(CN)_6]$ (5 mM); 300 W xenon lamp (λ ≥ 420 nm),0.5 h top-irradiation.

[b] Impregnation method.

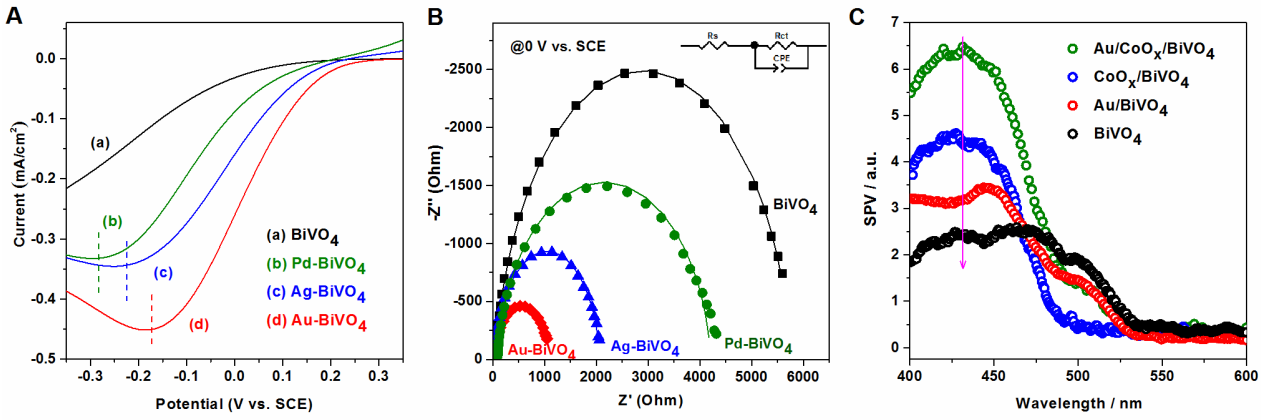


**Figure 3. The Functions of Cocatalysts and Promotion of Charge Separation with Dual-Cocatalys**

(A) Comparison of electrochemical linear sweep voltammetry (LSV) curves of typical samples in the PBS solution (pH=6.0 100 mM) containing 5 mM $K_3[Fe(CN)_6]$; (B) Comparison of electrochemical impedance spectra (EIS) of typical samples; (C) Comparison of surface photovoltage (SPV) spectra of typical samples (irradiated from 400 nm to 600 nm, with a 500 W xenon lamp).

Figure

Click here to access/download;Figure;Scheme 1-112.tif

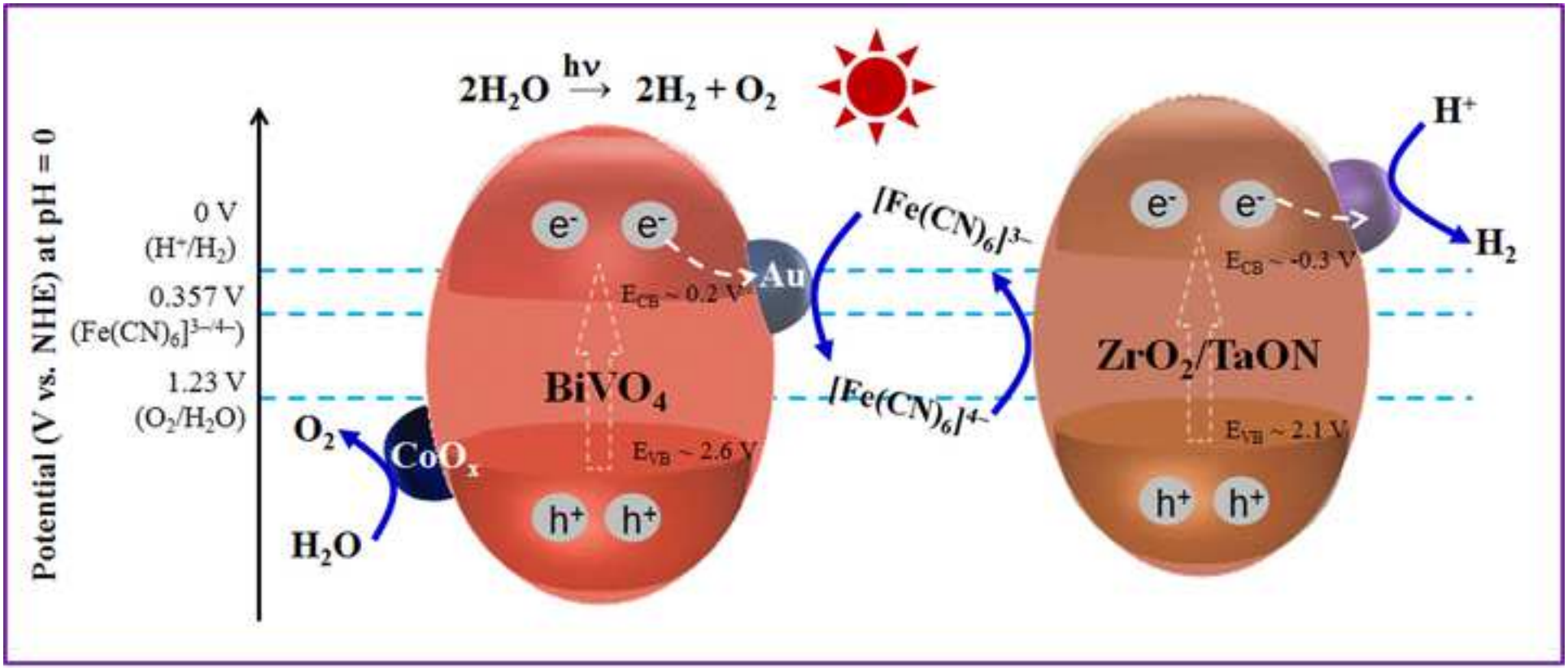

Figure

Click here to access/download;Figure;Figure 1-112.tif

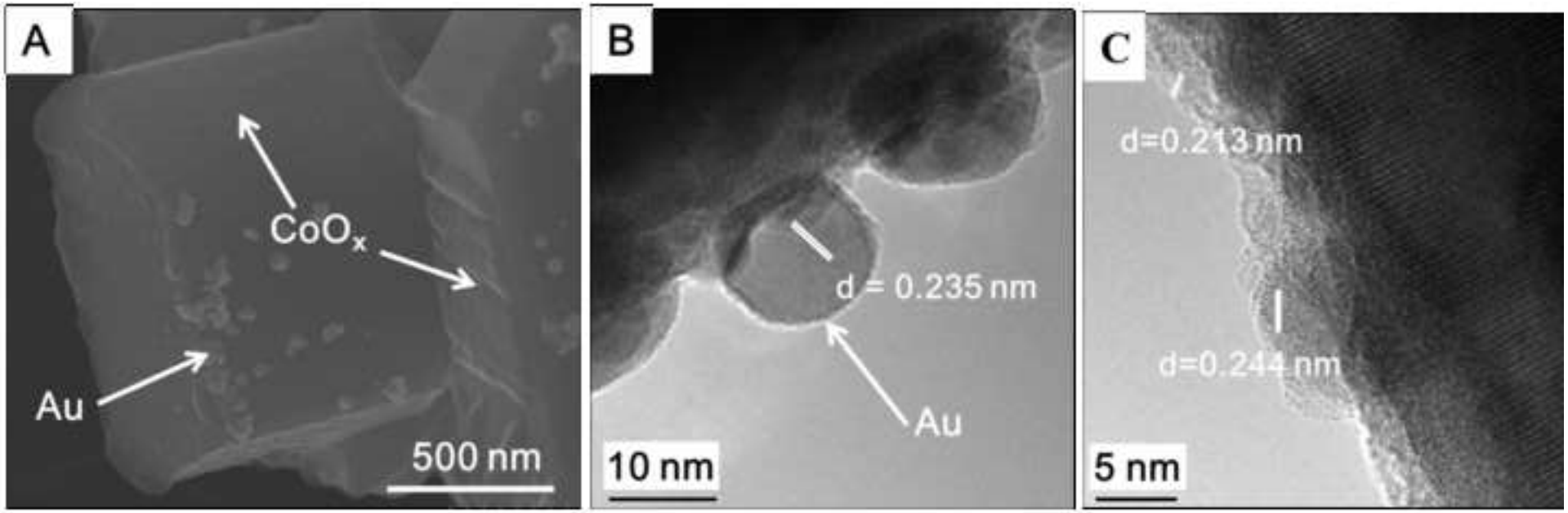

Figure

Click here to access/download;Figure;Figure 2-112.tif

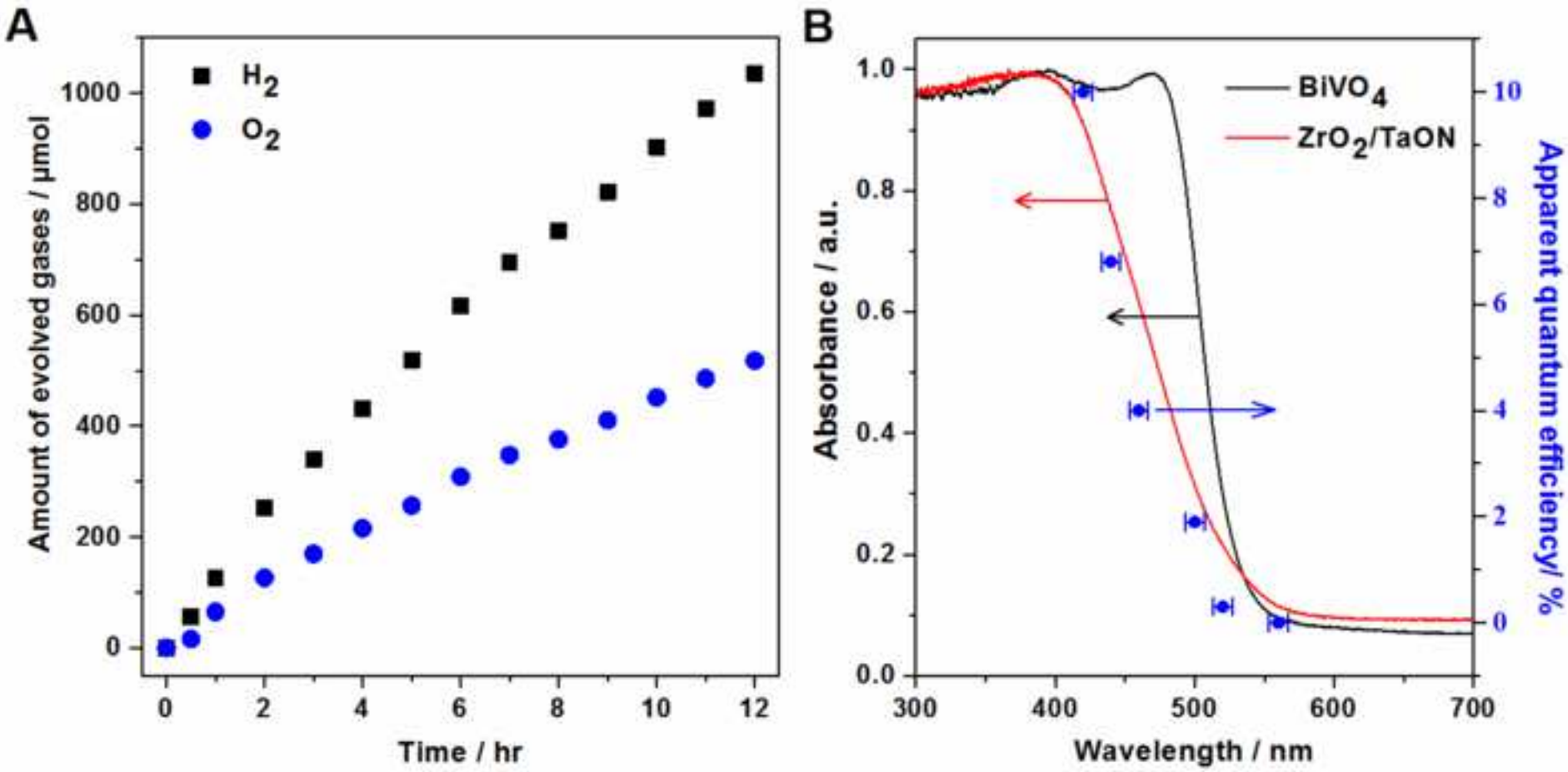

Figure

Click here to access/download;Figure;Figure 3-172.tif

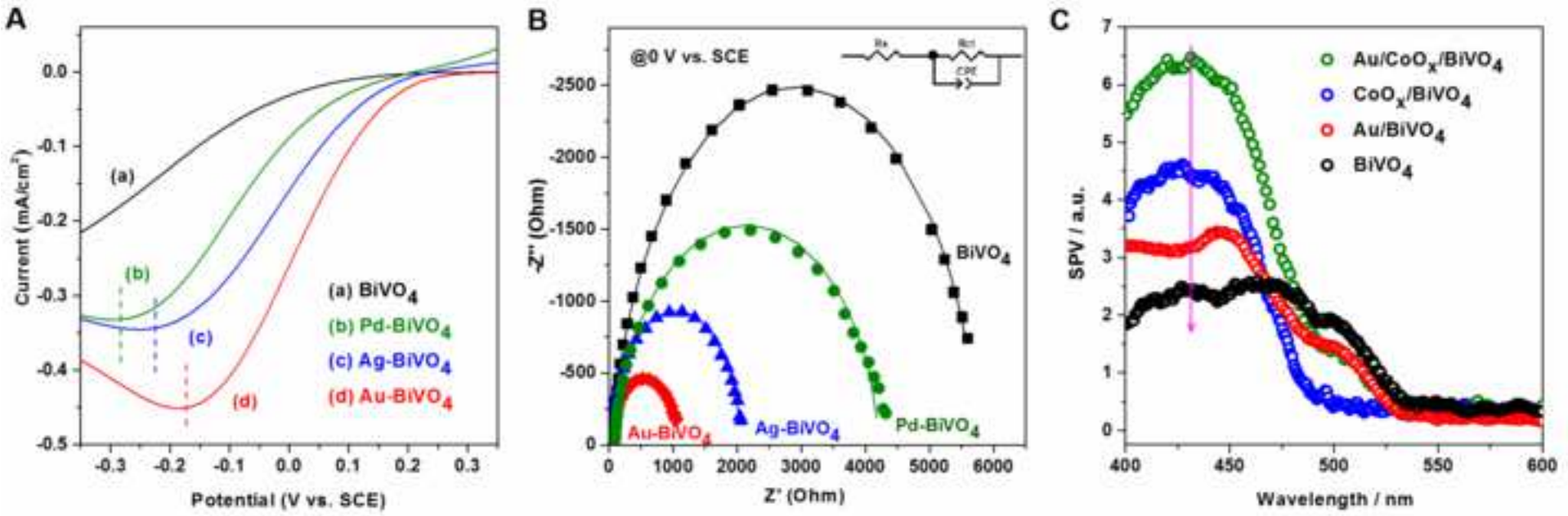

**Supplemental data items**

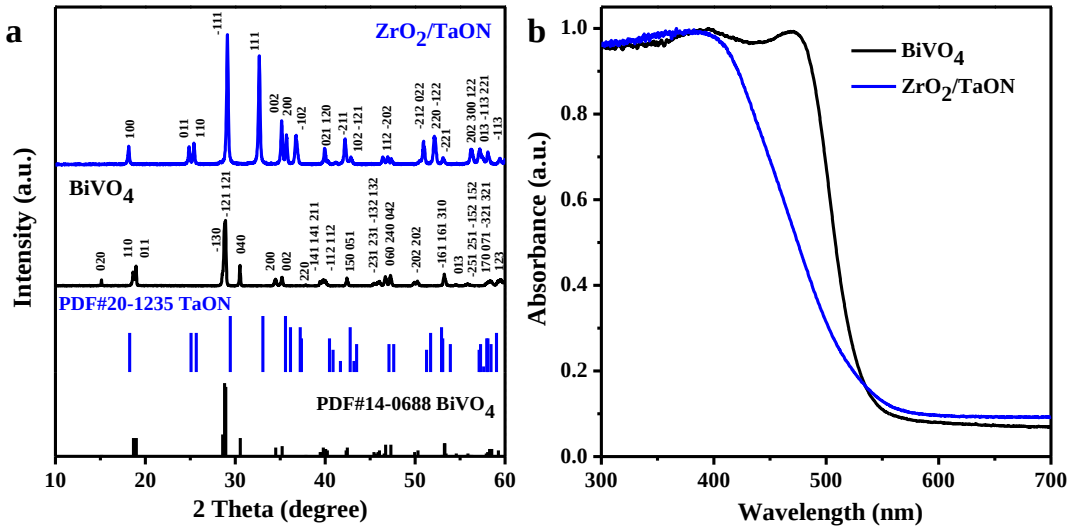


**Figure S1** Structural characterizations of $BiVO_4$ and $ZrO_2$/TaON samples: (a) XRD patterns and (b) UV-Vis DRS.

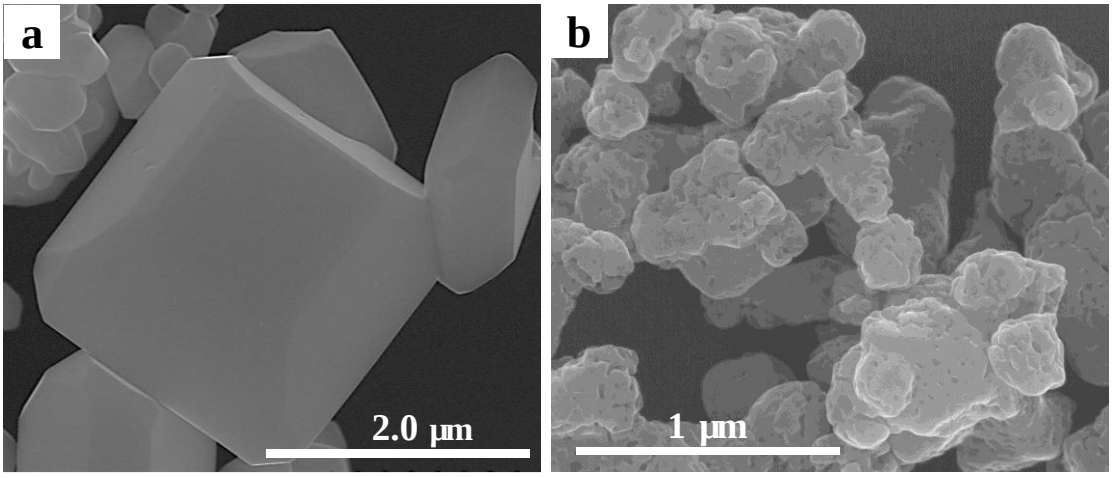


**Figure S2** FESEM images of typical samples: (a) $BiVO_4$; and (b) $ZrO_2$/TaON.

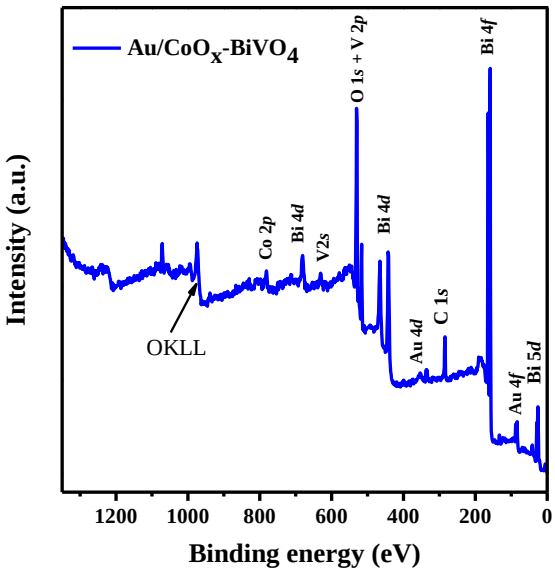


**Figure S3** The full sweep XPS spectrum of Au/$CoO_x$-$BiVO_4$ sample. Except for C element from the surroundings, only Au, Co, Bi, V and O elements can be found in the XPS spectrum.[1]

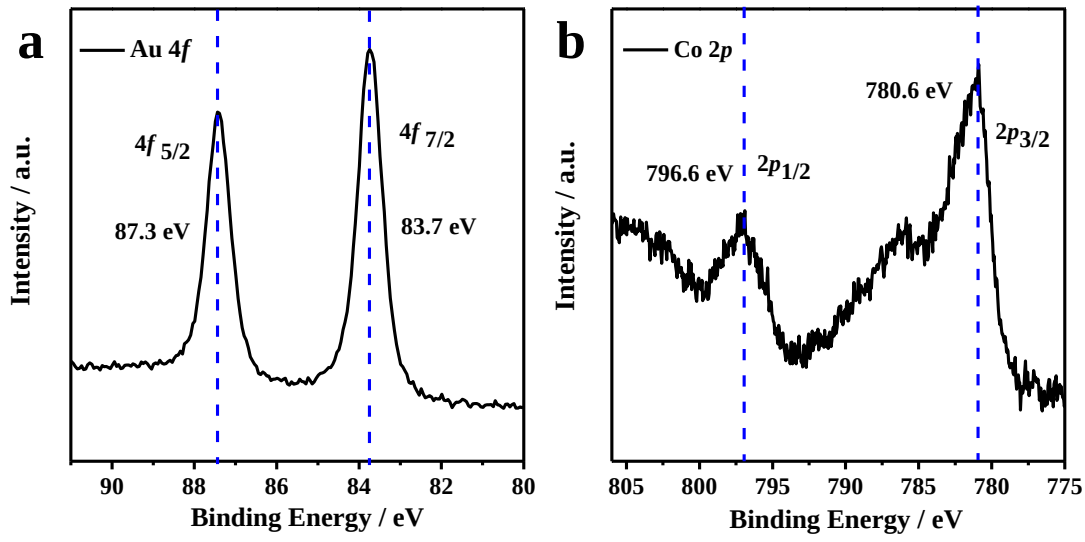


**Figure S4** XPS spectra of Au/$CoO_x$-$BiVO_4$ sample: (a) Au 4*f* ; and (b) Co 2*p*

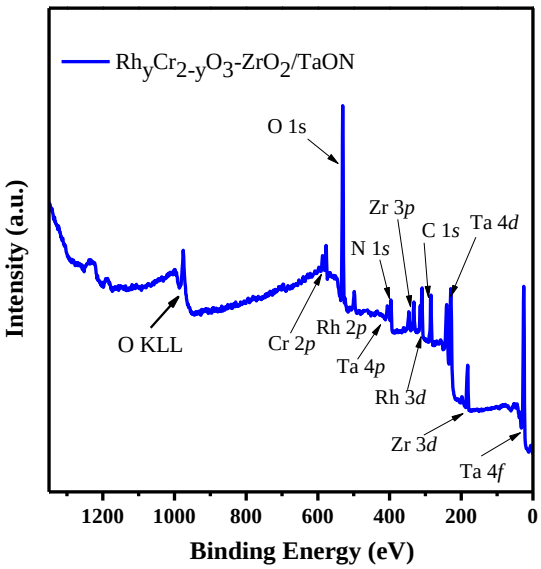


**Figure S5** The full sweep XPS spectrum of Rh$_y$Cr$_{2-y}$O$_3$-ZrO$_2$/TaON sample. Except for C element from the surroundings, only Rh, Cr, Zr, Ta, N and O elements can be found in the XPS spectrum.[2, 3]

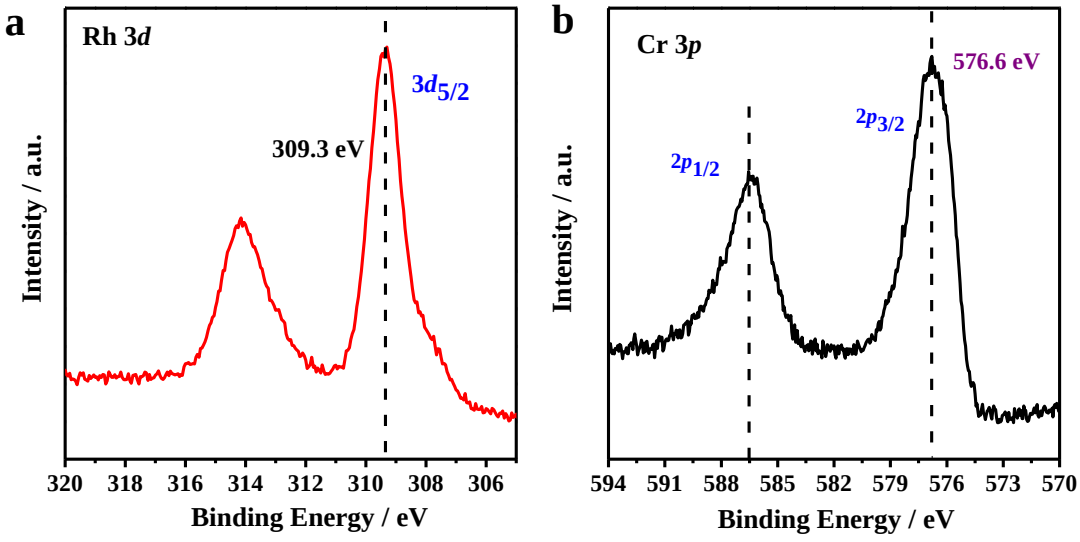


**Figure S6** XPS spectra of Rh$_y$Cr$_{2-y}$O$_3$-ZrO$_2$/TaON sample: (a) Rh 3*d*; and (b) Cr 3*p*.

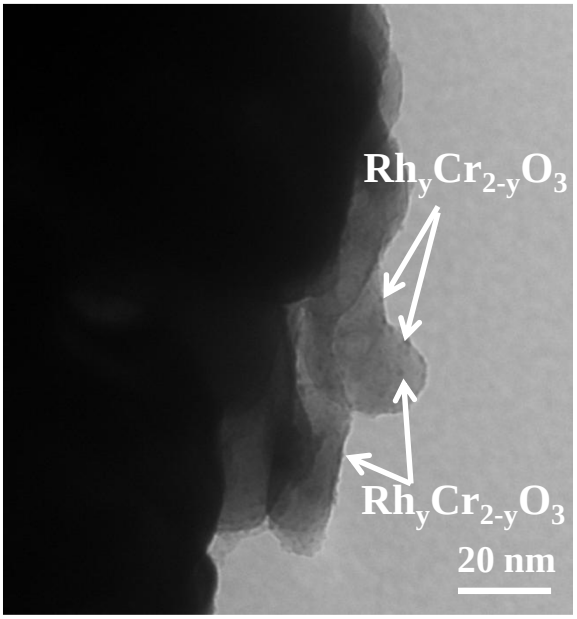


**Figure S7** Representative TEM image of $Rh_yCr_{2-y}O_3$-$ZrO_2$/TaON sample.

**Table S1.** Influence of cocatalyst and experimental conditions on the photocatalyitc Z-scheme overall water splitting performances under visible light irradiation

| entry | HEP | amount of HEP (mg) | OEP | amount of OEP (mg) | Concentration of shuttle ions (mM) | Initial activity (μmol/h) | |
|---|---|---|---|---|---|---|---|
| | | | | | | $H_2$ | $O_2$ |
| 1 | $Rh_yCr_{2-y}O_3$-$ZrO_2$/ TaON | 25 | Au-$BiVO_4$ | 75 | 5 | 53 | 27 |
| 2 | $Rh_yCr_{2-y}O_3$-$ZrO_2$/ TaON | 20 | $CoO_x$-$BiVO_4$ | 80 | 5 | 41 | 20 |
| 3 | $Rh_yCr_{2-y}O_3$-$ZrO_2$/ TaON | 50 | Au/$CoO_x$-$BiVO_4$ | 50 | 5 | 84 | 42 |
| 4 | $Rh_yCr_{2-y}O_3$-$ZrO_2$/ TaON | 50 | Au/$CoO_x$-$BiVO_4$ | 50 | 10 | 130 | 65 |
| 5 | $Rh_yCr_{2-y}O_3$-$ZrO_2$/ TaON | 50 | Au/$CoO_x$-$BiVO_4$ | 50 | 15 | 88 | 44 |
| 6 | $Rh_yCr_{2-y}O_3$-$ZrO_2$/ TaON | 50 | $BiVO_4$ | 50 | 10 | 108 | 5 |

Reaction conditions: $Rh_yCr_{2-y}O_3$-$ZrO_2$/TaON as HEP (1.0 *wt*% Rh and 1.5*wt*% Cr); $BiVO_4$ with cocatalyst modified as OEP; 25 mM sodium phosphate buffer solution (PBS pH = 6.0) containing different amount of $K_4[Fe(CN)_6]$; 300 W xenon lamp (λ ≥ 420 nm), Pyrex top-irradiation type.

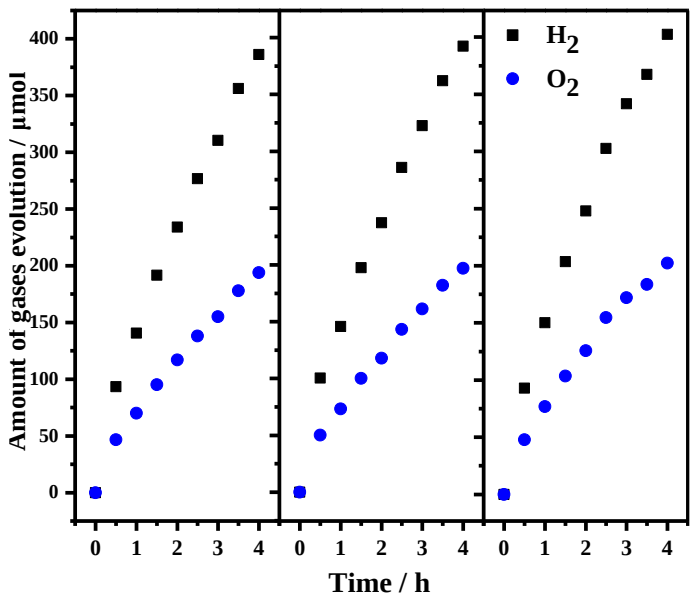


**Figure S8** Multiple cycles of Z-scheme overall water splitting using Au/$CoO_x$-$BiVO_4$ as the OEP and $Rh_yCr_{2-y}O_3$-$ZrO_2$/TaON as the HEP via $K_3[Fe(CN)_6]$/$K_4[Fe(CN)_6]$ redox mediator. Reaction conditions: 50 mg OEP (0.8 *wt*% Au; 0.1 *wt*% $CoO_x$), 50 mg HEP (1.0 *wt*% Rh, 1.5 *wt*% Cr), 100 mL 25 mM sodium phosphate buffer solution (PBS pH = 6.0) containing $K_4[Fe(CN)_6]$ (10 mM), 300 W xenon lamp (λ ≥ 420 nm), temperature: 288 K, Pyrex top-irradiation type.

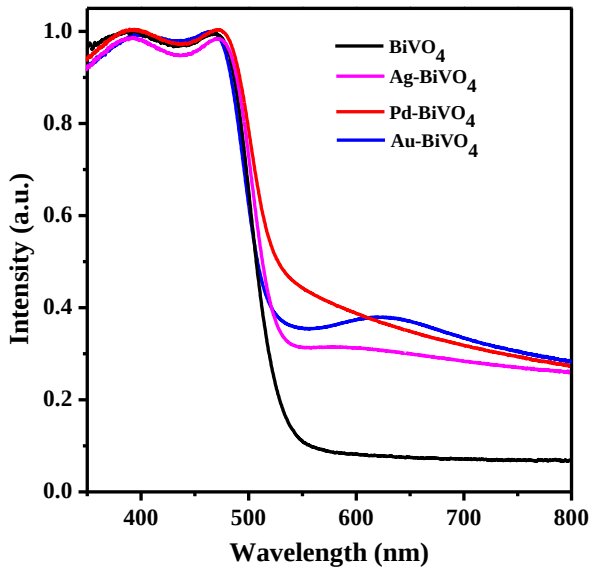


**Figure S9** The UV-vis DRS of $BiVO_4$ and different cocatalysts loaded $BiVO_4$ samples.

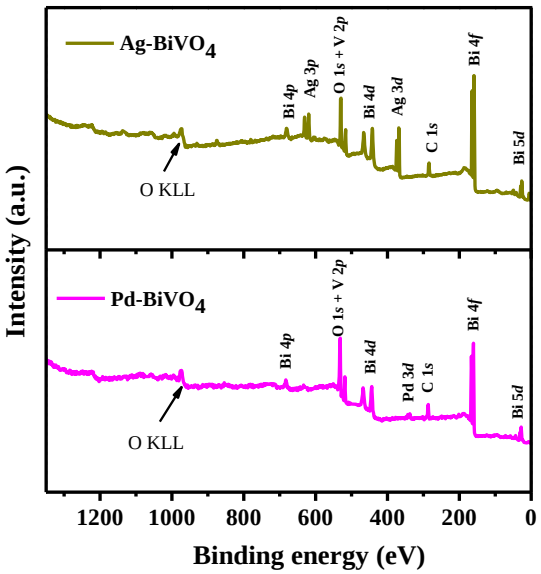


**Figure S10** The full sweep XPS spectrum of Ag-$BiVO_4$ and Pd-$BiVO_4$ samples. Except for C element from the surroundings, only Ag, Pd, Bi, V and O elements can be found in the XPS spectrum.

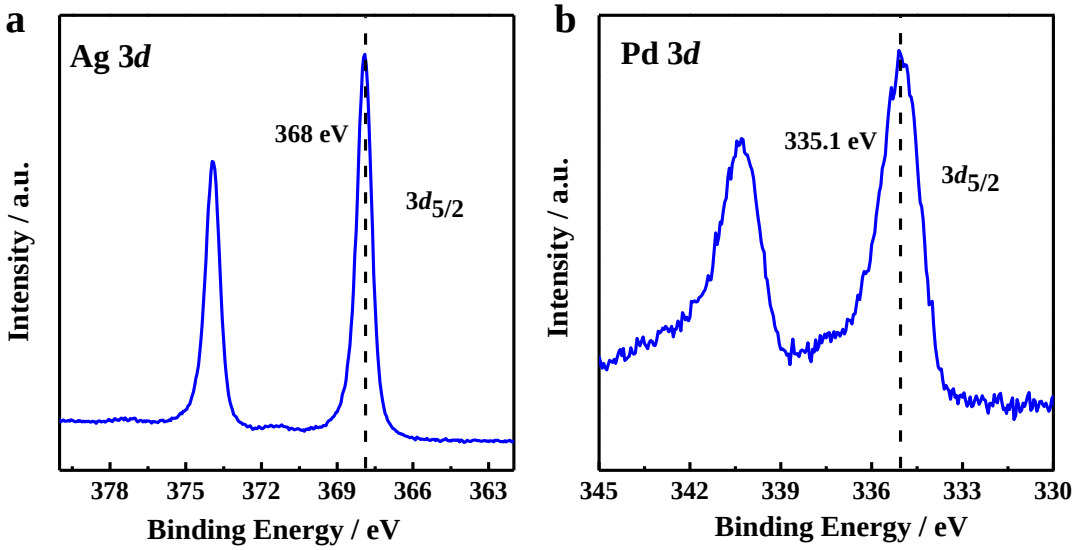


**Figure S11** XPS analysis of typical samples with different cocatalysts loaded: (a) Ag 3*d*; and (b) Pd 3*d*.

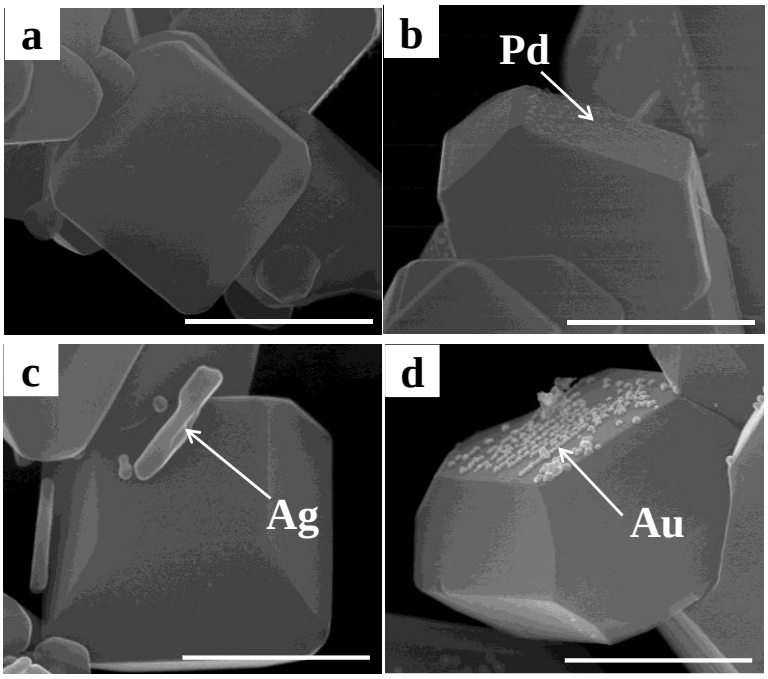


**Figure S12** Representative FESEM images of typical samples: (a) pristine $BiVO_4$; (b) Pd-$BiVO_4$; (c) Ag-$BiVO_4$; (d) Au-$BiVO_4$.
The contents of the deposited metals are all 0.8*wt*%. Scale bar, 1 μm.

**Table S2** Values of $R_s$ and $R_{ct}$ of different $BiVO_4$-based electrodes

| Entry | Photocatalysts | $R_s$ (Ohm) | $R_{ct}$ (Ohm) |
|---|---|---|---|
| 1 | $BiVO_4$/FTO | 42.7 | 5725 |
| 2 | Pd-$BiVO_4$/FTO | 27.1 | 4297 |
| 3 | Ag-$BiVO_4$/FTO | 27.9 | 2035 |
| 4 | Au-$BiVO_4$/FTO | 30.5 | 1038 |

**Table S3** Rates of $O_2$ evolution on the different photocatalysts loaded with Au as cocatalyst

| Entry | Photocatalysts | $O_2$ evolution rate (μmol/2h) |
|---|---|---|
| 1 | $WO_3$[a] | 0.6 |
| 2 | Au-$WO_3$[a] | 2.3 |
| 3 | $SrTiO_3$ | 1.3 |
| 4 | Au-$SrTiO_3$ | 2.6 |
| 5 | $TiO_2$(P25) | 7.6 |
| 6 | Au-$TiO_2$(P25) | 13.6 |

**Reaction conditions:** 20 mg photocatalyst; 0.8 *wt*% Au loaded; 20 mL 50 mM sodium phosphate buffer solution (PBS pH = 6.0) containing $K_3[Fe(CN)_6]$ (5 mM); 300 W xenon lamp, Pyrex top-irradiation type

[a] 300 W xenon lamp (λ ≥ 420 nm)

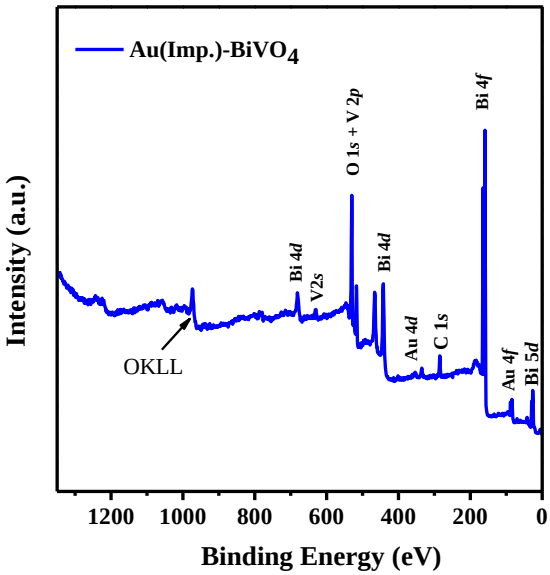


**Figure S13** The full sweep XPS spectrum of Au(Imp.)-$BiVO_4$ sample. Except for C element from the surroundings, only Au, Bi, V and O elements can be found in the XPS spectrum.

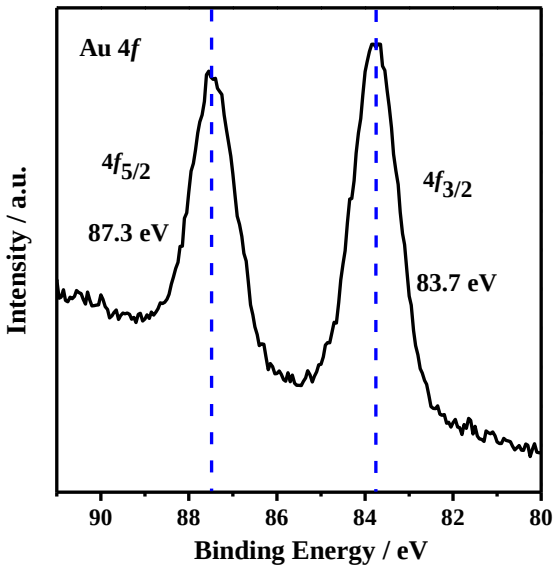


**Figure S14** Au 4*f* XPS spectra of Au(Imp.)-$BiVO_4$ sample

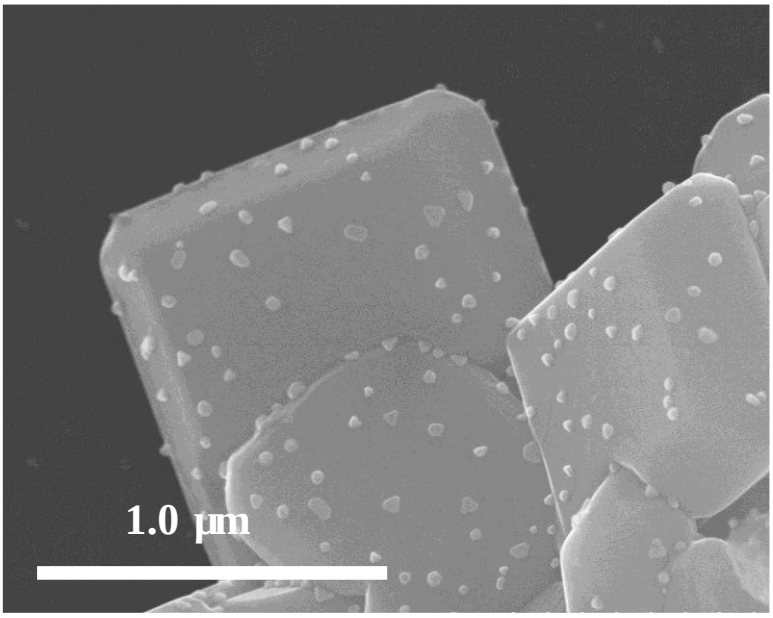


**Figure S15** Representative FESEM image of Au(Imp.)-$BiVO_4$.

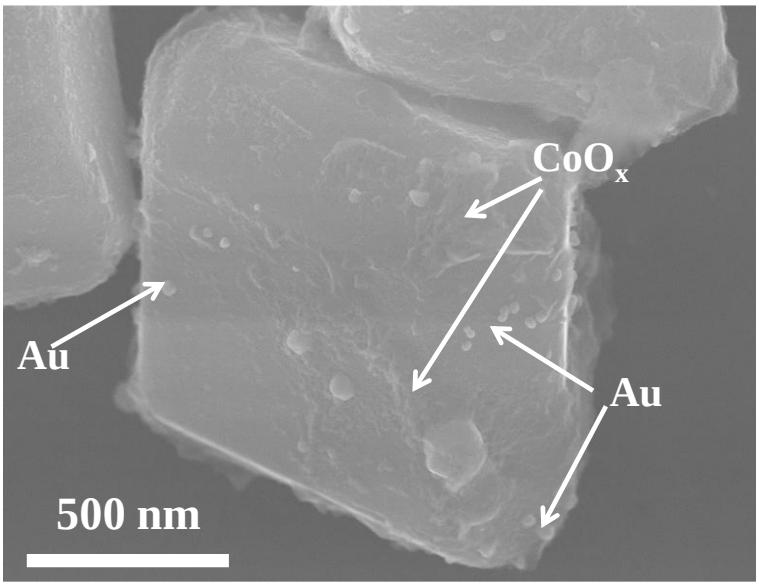


**Figure S16** Representative FESEM image of Au/$CoO_x$(Imp.)-$BiVO_4$ sample

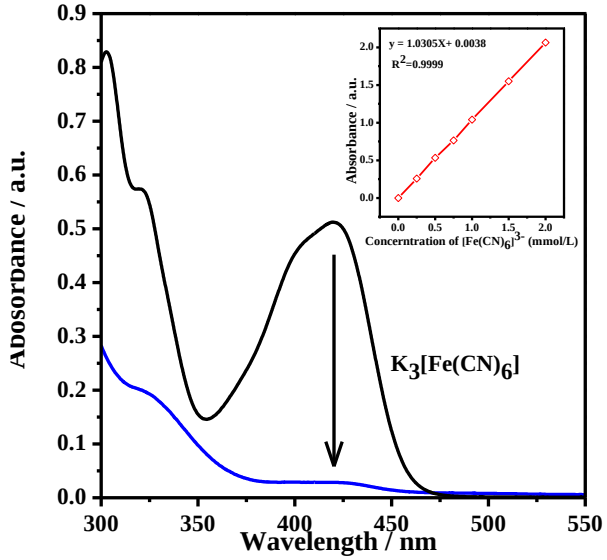


**Figure S17** UV-Vis spectra of $K_3[Fe(CN)_6]$ before and after the reaction.
**Reaction conditions:** 20 mg Au/$CoO_x$-$BiVO_4$; 20 mL 50 mM sodium phosphate buffer solution (PBS pH = 6.0) containing $K_3[Fe(CN)_6]$ (5 mM); 300 W xenon lamp (λ ≥ 420 nm), 1 h top-irradiation. Before the measurement, the solution was diluted 10 times.

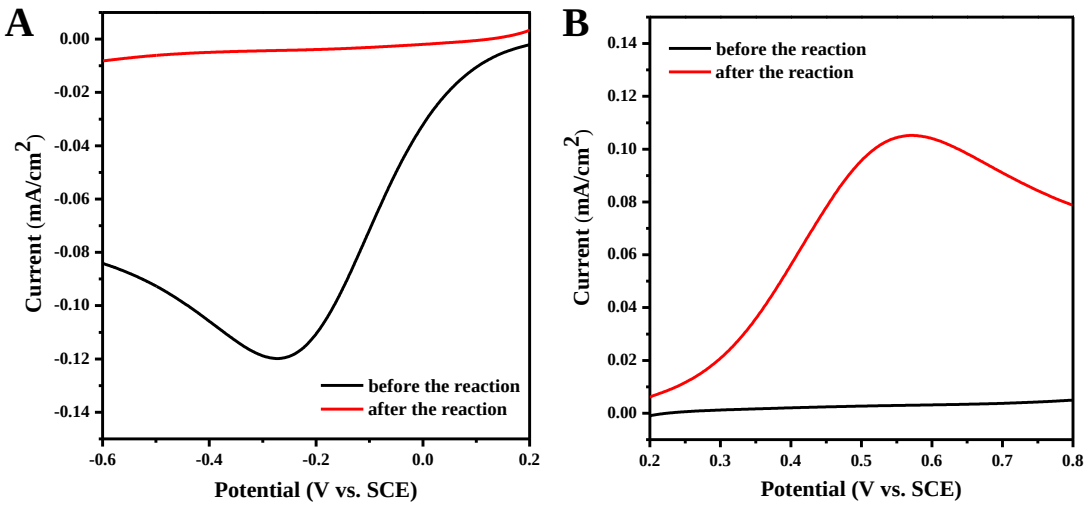


**Figure S18** The electrochemical linear sweep voltammetry (LSV) curves of the solution before and after the $O_2$-evolving reaction.

**Reaction conditions:** 20 mg Au/$CoO_x$-$BiVO_4$; 20 mL 50 mM sodium phosphate buffer solution (PBS pH = 6.0) containing $K_3[Fe(CN)_6]$ (5 mM); 300 W xenon lamp (λ ≥ 420 nm), 1 h top-irradiation.

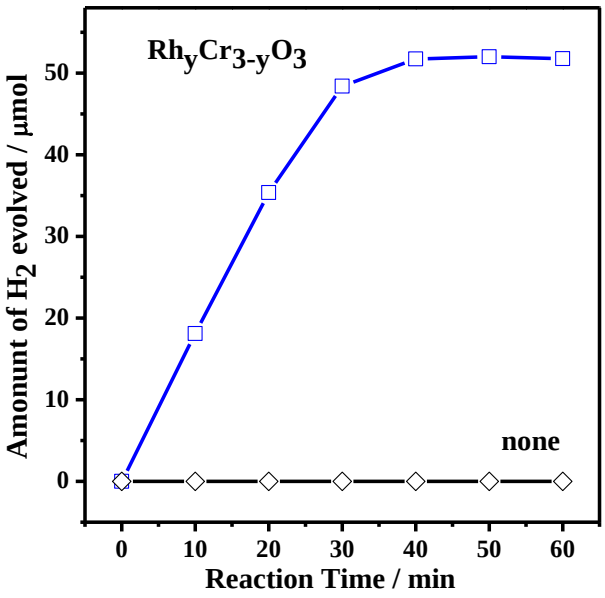


**Figure S19** Typical time courses of $H_2$ evolution on $Rh_yCr_{2-y}O_3$-$ZrO_2$/TaON and $ZrO_2$/TaON.

**Reaction conditions:** 20 mg photocatalyst; 1.0 *wt*% Rh and 1.5 *wt*% Cr; 20 mL 50 mM sodium phosphate buffer solution (PBS pH = 6.0) containing $K_4[Fe(CN)_6]$ (5 mM); 300 W xenon lamp (λ ≥ 420 nm), Pyrex top-irradiation type.

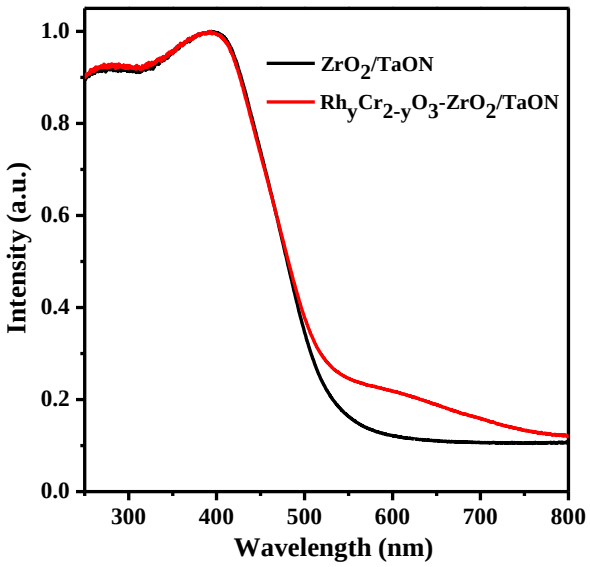


**Figure S20** The UV-vis DRS of $ZrO_2$/TaON and $Rh_yCr_{2-y}O_3$-$ZrO_2$/TaON samples.

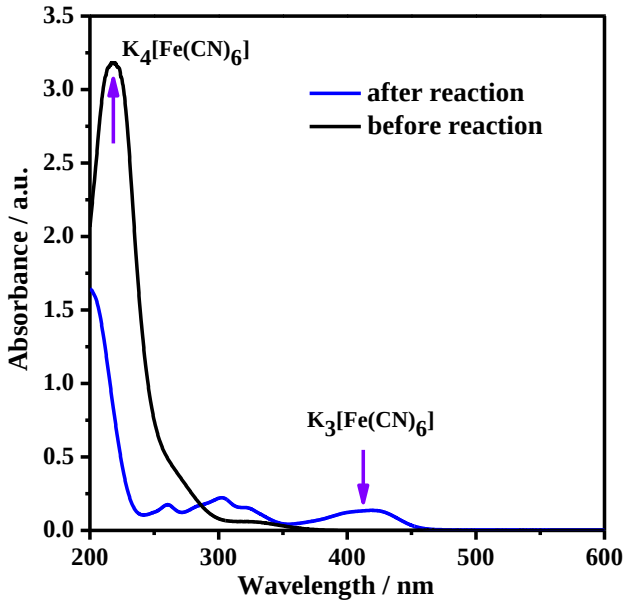


**Figure S21** UV-Vis spectra of $K_4[Fe(CN)_6]$ before and after the reaction.
**Reaction conditions:** 20 mg $Rh_yCr_{2-y}O_3$-$ZrO_2$/TaON; 1.0 *wt*% Rh and 1.5 *wt*% Cr; 20 mL 50 mM sodium phosphate buffer solution (PBS pH = 6.0) containing $K_4[Fe(CN)_6]$ (5 mM); 300 W xenon lamp (λ ≥ 420 nm), 1 h top-irradiation. Before the measurement, the solution was diluted 40 times.

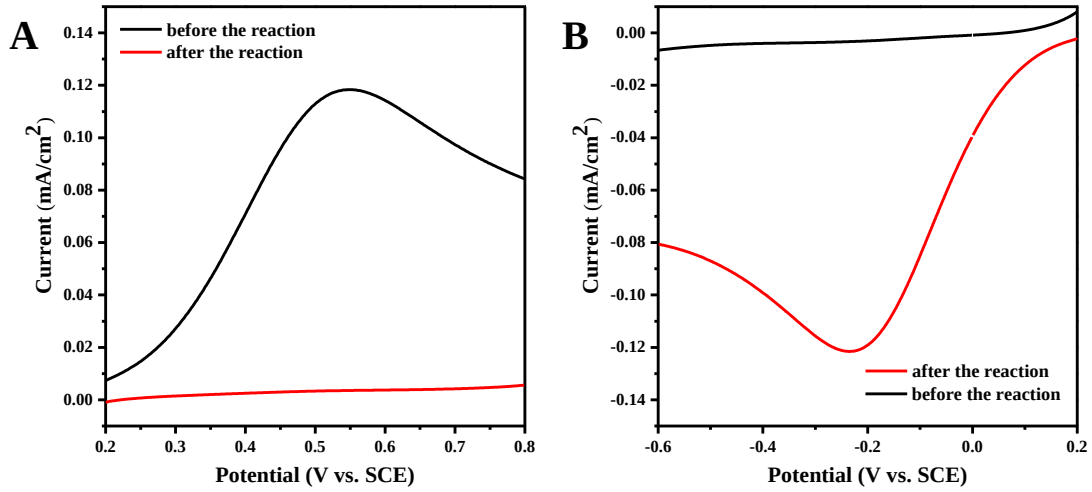


**Figure S22** The electrochemical linear sweep voltammetry (LSV) curves of the solution before and after the $H_2$-evolving reaction.

**Reaction conditions:** 20 mg $Rh_yCr_{2-y}O_3$-$ZrO_2$/TaON; 1.0 *wt*% Rh and 1.5 *wt*% Cr; 20 mL 50 mM sodium phosphate buffer solution (PBS pH = 6.0) containing $K_4[Fe(CN)_6]$ (5 mM); 300 W xenon lamp (λ ≥ 420 nm), 1 h top-irradiation.

**Table S4** Representative redox-based visible-light-driven Z-scheme overall water-splitting systems.

| HEP | OEP | Electron mediator | Light source | Reactant solution | Efficiency | Refs |
|---|---|---|---|---|---|---|
| Pt/$SrTiO_3$:Cr/Ta | $PtO_x/WO_3$ | $IO_3^-/I^-$ | 300 W Xe lamp (>420 nm) | $H_2O$ | AQE: 0.1% at 420 nm | [4] |
| Pt/TaON | $PtO_x/WO_3$ | $IO_3^-/I^-$ | 300 W Xe lamp (>420 nm) | $H_2O$ | AQE: 0.4% at 420 nm | [5] |
| Pt/$CaTaO_2N$ | $PtO_x/WO_3$ | $IO_3^-/I^-$ | 300 W Xe lamp (>420 nm) | $H_2O$ | No data | [6] |
| Pt/$BaTaO_2N$ | $PtO_x/WO_3$ | $IO_3^-/I^-$ | 300 W Xe lamp (>420 nm) | $H_2O$ | AQE: ~0.1% at 420 nm | [6] |
| Pt/$BaZrO_3$/$BaTaO_2N$ | $PtO_x/WO_3$ | $IO_3^-/I^-$ | 300 W Xe lamp (>420 nm) | $H_2O$ | No data | [7] |
| Pt/$BaTaO_2N$ /$Ta_3N_5$ | $PtO_x/WO_3$ | $IO_3^-/I^-$ | 300 W Xe lamp (>420 nm) | $H_2O$ | AQE: 0.1% at 420 nm | [8] |
| Pt/$BaTiO_3$:Rh | $PtO_x/WO_3$ | $IO_3^-/I^-$ | 300 W Xe lamp (>420 nm) | $H_2O$ | AQE: 0.5% at 420 nm | [9] |
| Pt/TaON | $RuO_2/ZrO_2$ /TaON | $IO_3^-/I^-$ | 300 W Xe lamp (>420 nm) | $H_2O$ | AQE: 0.1%-0.2% at 420 nm | [10] |
| Pt/$ZrO_2$/TaON | Ir/$TiO_2$/$Ta_3N_5$ | $IO_3^-/I^-$ | 300 W Xe lamp (>420 nm) | $H_2O$ | No data | [11] |
| Pt/$ZrO_2$/TaON | $PtO_x/WO_3$ | $IO_3^-/I^-$ | 300 W Xe lamp (>420 nm) | $H_2O$ | AQE: 6.3% at 420 nm | [12] |

| | | | | | | |
|---|---|---|---|---|---|---|
| $Pt/MgTa_2O_{6-x}N_y/TaON$ | $PtO_x/WO_3$ | $IO_3^-/I^-$ | 300 W Xe lamp (>420 nm) | $H_2O$ | AQE: 6.8% at 420 nm | [13] |
| $Pt/SrTiO_3$:Cr/Ta | H-Cs-$WO_3$ | $IO_3^-/I^-$ and $I_3^-/I^-$ | 300 W Xe lamp (>420 nm) | $H_2O$ | AQE: 1.5% at 420 nm | [14] |
| $Pt\text{-}IrO_2/Sm_2Ti_2S_2O_5$ | $PtO_x$/H-Cs-$WO_3$ | $I_3^-/I^-$ | 300 W Xe lamp (>420 nm) | $H_2O$ | STH: 0.003% | [15] |
| Dye-adsorbed $Pt/H_4Nb_6O_{17}$ | $IrO_2$-$PtO_x/WO_3$ | $I_3^-/I^-$ | 300 W Xe lamp (>420 nm) | pH = 4.5 | AQE: 0.05% at 480 nm for H2 evolution | [16] |
| $Pt/g\text{-}C_3N_4$ | $PtO_x/WO_3$ or $BiVO_4$ | $I_3^-/I^-$ or $Fe^{3+}/Fe^{2+}$ | 300 W Xe lamp (>420 nm) | $H_2O$ (pH = 8.3) or $H_2O$ (pH = 3.0, $H_2SO_4$ mediated) | No data | [17] |
| $Pt/SrTiO_3$:Rh | $Bi_2MoO_6$ | $Fe^{3+}/Fe^{2+}$ | 300 W Xe lamp (>420 nm) | pH = 2.4, $H_2SO_4$ mediated | AQE: 0.2% at 420 nm | [18] |
| $Pt/SrTiO_3$:Rh | $WO_3$ | $Fe^{3+}/Fe^{2+}$ | 300 W Xe lamp (>420 nm) | pH = 2.4, $H_2SO_4$ mediated | AQE: 0.5% at 420 nm | [18] |
| $Ru/SrTiO_3$:Rh | $BiVO_4$ | $Fe^{3+}/Fe^{2+}$ | 300 W Xe lamp (>420 nm) | pH = 2.4, $H_2SO_4$ mediated | AQE: 4.2% at 420 nm, STH: 0.1% | [19] |
| $Ru/SrTiO_3$:Rh | $Bi_4NbO_8Cl$ | $Fe^{3+}/Fe^{2+}$ | 300 W Xe lamp (>420 nm) | pH = 2.5, HCl mediated | AQE: 0.4% at 420 nm for O2 evolution | [20] |
| $Ru/SrTiO_3$:Rh or $Ru_2S_3/CdS$ | Photosystem II | $Fe(CN)_6^{3-/4-}$ | 300 W Xe lamp (>420 nm) | $H_2O$ (50 mM sodium phosphates, 15 mM NaCl, pH = 6.0 or 7.0) | No data | [21] |
| $Pt/SrTiO_3$:Rh | $BiVO_4$ | $[Co(bpy)_3]^{3+/2+}$ or $[Co(phen)_3]^{3+/2+}$ | 300 W lamp (>420 nm) | $H_2O$ | AQE: 2.1% at 420 nm | [22] |
| $Ru/(CuGa)_{0.8}Zn_{0.4}S_2$ | $BiVO_4$ | $[Co(terpy)_3]^{3+/2+}$ | 300 W lamp (>420 nm) | $H_2O$ | STH: 0.0025% | [23] |
| $Ru/SrTiO_3$:Rh | $WO_3$ | $[SiW_{11}O_{39}Mn^{III}(H_2O)]^{5-}/[SiW_{11}O_{39}Mn^{II}(H_2O)]^{6-}$ | 300 W lamp (>420 nm) | $H_2O$ (0.25 M phosphate solution, pH = 4.3) | AQE: 0.24% at 400 nm for H2 evolution AQE: 0.36% at 400 nm for O2 evolution | [24] |
| $Ru/SrTiO_3$:Rh | Fe−H−Cs−$WO_3$ | $VO_2^+/VO^{2+}$ | 300 W lamp (>420 nm) | pH = 2.4, | STH: 0.06% | [25] |
| $Rh_yCr_{2-y}O_3$-$ZrO_2/TaON$ | Au/$CoO_x$-$BiVO_4$ | $Fe(CN)_6^{3-/4-}$ | 300 W Xe lamp (>420 nm) | $H_2O$ (25 mM $Na_3PO_4$, pH = 6.0) | AQE: 10.3% at 420 nm, STH: ~0.5% | This work |

**Supplemental Experimental Productions**

**Materials and reagents.**

For the preparation of $ZrO_2$-modified TaON and $BiVO_4$ samples, $Ta_2O_5$ (99.9%, High Purity Chemicals), $ZrO(NO_3)_2{\cdot}2H_2O$ ($ZrO_2$ 45.0%, Guangfu Chemical Reagent), $Bi(NO_3)_3{\cdot}5H_2O$ (99.0%, Sinopharm Chemical), and $NH_4VO_3$ (99.0%, Sinopharm Chemical) were used. $Na_3RhCl_6{\cdot}12H_2O$ (Rh 17.1%, Alfa Aesar), $HAuCl_4$ (Au 49%, Sinopharm Chemical),

$CoSO_4 \cdot 7H_2O$ (99.5%, Sinopharm Chemical), $Na_2PdCl_4$ (98%, Aladdin), $AgNO_3$ (99.9%, Alfa Aesar) and $K_2CrO_4$ (99.5% Kermal Chemical Reagent) were employed as the precursors of cocatalysts. Methanol (99.5%, Sinopharm Chemical) and $K_4[Fe(CN)_6] \cdot 3H_2O$ (99.5%, Sinopharm Chemical) were used as hole acceptors. $K_3[Fe(CN)_6]$ (99.5%, Sinopharm Chemical) was used as electron donors. The commercial $TiO_2$ (P25, Alfa Aesar), $WO_3$ (99.9%, High Purity Chemicals) and $SrTiO_3$ (99.9%, Alfa Aesar) was also used. All chemicals were used as-purchased without further purification.

**Characterizations of samples.**

XRD measurement was carried out on a Rigaku D/Max-2500/PC powder diffractometer (Cu Ka radiation) with an operating voltage of 40 kV and an operating current of 200 mA. The scan rate of 5° $min^{-1}$ was applied in the range of 10–60° at a step size of 0.02°. UV-Vis diffuse reflectance spectra (DRS) were recorded on a UV-Vis spectrophotometer (JASCO V-550) equipped with an integrating sphere, and $BaSO_4$ powder was used as the reference for baseline correction. The morphologies and particle sizes were examined by high-resolution scanning electron microscopy (FESEM; S-5500, Hitachi) taken with a Quanta 200 FEG scanning electron microscope, transmission electron microscopy (TEM; HT7700, Hitachi) and high-resolution transmission electron microscopy (HRTEM; JEOL JEM-2000EX). The binding energies were determined by X-ray photoelectron spectroscopy (XPS, Thermo Esclab 250Xi, a monochromatic Al Ka X-ray source), and calibrated by the C 1s peak (284.6 eV) for each sample. Kelvin Probe Force Microscopy (KPFM) was carried out in Lift mode with a lift height of 100nm. The Pt/Ir coated Si tip was used as Kelvin tip with spring constant of 1-5N/m and resonant frequency of 60-100KHZ. To acquire the surface photovoltage (SPV) spectroscopy,

the outgoing monochromatic light was splitted out from the light of 500 W Xenon-arc lamp by a Zolix Omni-λ 500 monochromator and was focused on the sample by lens with a fixed low grazing angle, which ensures sample under the measuring AFM tip was properly illuminated. To quantify the transient SPV signals, the varied surface potential signals are fed to a Stanford SR 830 lock-in amplifier, and synchronized with the chopped signals. The loading amounts of Rh and Cr elements on the surface of $ZrO_2$/TaON are determined to be 0.96 *wt*% and 1.54 *wt*% by inductively coupled plasma atomic emission spectrometer (ICP-AES), respectively.

**Photocatalytic tests.**

The photocatalytic reactions were carried out in a Pyrex top irradiation-type reaction vessel connected to a closed gas circulation system. Prior to photo-irradiation, the reaction mixture was evacuated to ensure the completed air removal, and then irradiated from the top side with a 300 W Xenon lamp using a filtration mirror (Hoya, L-42; λ ≥ 420 nm) to cut off the light in the ultraviolet region. A flow of cooling water was used to maintain the reaction mixture at room temperature. The evolved gases were analyzed by gas chromatography (Agilent; GC-7890A, MS-5A column, TCD, Ar carrier).

**Measurements of apparent quantum efficiency (AQE) and solar-to-energy (STH) energy conversion efficiency.**

The AQE was measured using a Pyrex top-irradiation-type reaction vessel and a 300 W xenon lamp fitted with a 420 nm band-pass filter (ZBPA420, Asahi Spectra Co., FWHM: 10 nm). The number of photons reaching the solution was measured using a calibrated Si photodiode (LS-100, EKO Instruments Co., LTD.), and the AQE ($\Phi$) was calculated using the following equation:

$$\phi(\%) = (AR / I) \times 100 \quad (1)$$

where *A*, *R*, and *I* are a coefficient, the A represents a coefficient (4 for $H_2$ evolution; 8 for $O_2$ evolution) and R represents the evolution rate of $H_2$ or $O_2$ in the initial one hour irradiation. The total number of incident photons at the wavelength of 420 nm, 440 nm, 460 nm, 480 nm, 500 nm and 560 nm were measured to be 2.8 × $10^{20}$ photons $h^{-1}$, 4.8 × $10^{20}$ photons $h^{-1}$, 6.5× $10^{20}$ photons $h^{-1}$, 7.1 × $10^{20}$ photons $h^{-1}$, 4.8 × $10^{20}$ photons $h^{-1}$ and 6.9 × $10^{20}$ photons $h^{-1}$, respectively. The evolution rates of $H_2$ under the wavelength of 420 nm, 440 nm, 460 nm, 480 nm, 500 nm and 560 nm were tested to be 12.0 umol $h^{-1}$, 13.6 umol $h^{-1}$, 10.1 umol $h^{-1}$, 7.5 umol $h^{-1}$, 3.7 umol $h^{-1}$, 0 umol $h^{-1}$, respectively.

The STH energy onversion efficiency ($\eta$) was calculated according to the following equation:

$$\eta(\%) = (R_H \times \Delta G^{\circ}) / (P \times S) \times 100 \quad (2)$$

where $R_H$, ΔG°, *P*, and *S* denote the rate of $H_2$ evolution (mol $s^{-1}$) in photocatalytic water splitting, standard Gibbs energy of water (237.13 × $10^3$ J $mol^{-1}$), intensity of simulated sunlight (0.1 W $cm^{-2}$) and irradiation area (4.0 $cm^2$), respectively. The light source was an AM 1.5G solar simulator (XES-40S2-CE, San-Ei Electric), and a top-irradiation reaction vessel was used. Photocatalytic Z-scheme overall water splitting activity was evaluated in 100 mL $K_4[Fe(CN)_6]$ aqueous solution (10 mM) with 50 mg 1.0 *wt*% $Rh_yCr_{2-y}O_3$-$ZrO_2$/TaON and 50 mg 0.8 *wt*% Au/0.1 *wt*% $CoO_x$-$BiVO_4$.

**Electrochemcial tests**.

As for the linear sweep voltammetry (LSV) and electrochemical impedance spectra (EIS) test, a platinum plate was used as a counter electrode and the saturated calomel electrode (SCE) as the reference electrode. The phosphate buffer solution (pH=6, 0.1 M) with 5 mM

$K_3[Fe(CN)_6]$ aqueous solution were used as an electrolyte. The potential of the working electrode was controlled by a potentiostat (Iviumstat, Ivium Technologies). Before the measurement, the solution was purged with argon gas. The Nyquist plots calculated from EIS were performed at 0 $V_{SCE}$ from 100000 to 0.1 Hz. Data were fit using Zview software. The transformation between $K_3[Fe(CN)_6]$ and $K_4[Fe(CN)_6]$ before and after the reaction was further proved by the linear sweep voltammetry (LSV). The glassy carbon electrode was used as the working electrode, and a platinum wire was used as a counter electrode together with the saturated calomel electrode (SCE) as the reference electrode.

**Supplemental References**


[1] N. Tian, H. Huang, Y. He, Y. Guo, T. Zhang, Y. Zhang, Mediator-free direct Z-scheme photocatalytic system: $BiVO_4$/g-$C_3N_4$ organic-inorganic hybrid photocatalyst with highly efficient visible-light-induced photocatalytic activity, Dalton Transactions, 44 (2015) 4297-4307.
[2] Z. Wang, J. Wang, J. Hou, K. Huang, S. Jiao, H. Zhu, Facile synthesis of efficient photocatalytic tantalum nitride nanoparticles, Materials Research Bulletin, 47 (2012) 3605-3611.
[3] K. Maeda, H. Terashima, K. Kase, M. Higashi, M. Tabata, K. Domen, Surface Modification of TaON with Monoclinic $ZrO_2$ to Produce a composite photocatalyst with enhanced hydrogen evolution activity under visible light, Bulletin of the Chemical Society of Japan, 81 (2008) 927-937.
[4] K. Sayama, K. Mukasa, R. Abe, Y. Abe, H. Arakawa, Stoichiometric water splitting into $H_2$ and $O_2$ using a mixture of two different photocatalysts and an $IO_3^-/I^-$ shuttle redox mediator under visible light irradiation, Chemical Communications, (2001) 2416-2417.
[5] R. Abe, T. Takata, H. Sugihara, K. Domen, Photocatalytic overall water splitting under visible light by TaON and $WO_3$ with an $IO_3^-/I^-$ shuttle redox mediator, Chemical Communications, (2005) 3829-3831.
[6] M. Higashi, R. Abe, K. Teramura, T. Takata, B. Ohtani, K. Domen, Two step water splitting into $H_2$ and $O_2$ under visible light by $ATaO_2N$ (A=Ca, Sr, Ba) and $WO_3$ with $IO_3^-/I^-$ shuttle redox mediator, Chemical Physics Letters, 452 (2008) 120-123.
[7] K. Maeda, D. Lu, K. Domen, Solar-driven Z-scheme water splitting using modified $BaZrO_3$–$BaTaO_2N$ solid solutions as photocatalysts, ACS Catalysis, 3 (2013) 1026-1033.
[8] Y. Qi, S. Chen, M. Li, Q. Ding, Z. Li, J. Cui, B. Dong, F. Zhang, C. Li, Achievement of visible-light-driven Z-scheme overall water splitting using barium-modified $Ta_3N_5$ as a $H_2$-evolving photocatalyst, Chemical Science, 8 (2017) 437-443.
[9] K. Maeda, Rhodium-doped barium titanate perovskite as a stable p-type semiconductor

photocatalyst for hydrogen evolution under visible light, ACS Applied Materials & Interfaces, 6 (2014) 2167-2173.
[10] M. Higashi, R. Abe, A. Ishikawa, T. Takata, B. Ohtani, K. Domen, Z-scheme overall water splitting on modified-TaON photocatalysts under visible light (λ<500 nm), Chemistry Letters, 37 (2007) 138-139.
[11] M. Tabata, K. Maeda, M. Higashi, D. Lu, T. Takata, R. Abe, K. Domen, Modified $Ta_3N_5$ powder as a photocatalyst for $O_2$ Eeolution in a two-step water splitting system with an iodate/iodide shuttle redox mediator under visible light, Langmuir, 26 (2010) 9161-9165.
[12] K. Maeda, M. Higashi, D. Lu, R. Abe, K. Domen, Efficient nonsacrificial water splitting through two-step photoexcitation by visible light using a modified oxynitride as a hydrogen evolution photocatalyst, Journal of the American Chemical Society, 132 (2010) 5858-5868.
[13] S. Chen, Y. Qi, T. Hisatomi, Q. Ding, T. Asai, Z. Li, K. Ma Su Su, F. Zhang, K. Domen, C. Li, Efficient Visible-light-driven Z-scheme overall water splitting using a $MgTa_2O_{6-x}N_y$/TaON heterostructure photocatalyst for $H_2$ evolution, Angewandte Chemie International Edition, 54 (2015) 8498-8501.
[14] Y. Miseki, S. Fujiyoshi, T. Gunji, K. Sayama, Photocatalytic water splitting under visible light utilizing $I_3^-/I^-$ and $IO_3^-/I^-$ redox mediators by Z-scheme system using surface treated $PtO_x/WO_3$ as $O_2$ evolution photocatalyst, Catalysis Science & Technology, 3 (2013) 1750-1756.
[15] G. Ma, S. Chen, Y. Kuang, S. Akiyama, T. Hisatomi, M. Nakabayashi, N. Shibata, M. Katayama, T. Minegishi, K. Domen, Visible light-driven Z-scheme water splitting using oxysulfide $H_2$ evolution photocatalysts, The Journal of Physical Chemistry Letters, 7 (2016) 3892-3896.
[16] R. Abe, K. Shinmei, N. Koumura, K. Hara, B. Ohtani, Visible-light-induced water splitting based on two-step photoexcitation between dye-sensitized layered niobate and tungsten oxide photocatalysts in the presence of a triiodide/iodide shuttle redox mediator, Journal of the American Chemical Society, 135 (2013) 16872-16884.
[17] D.J. Martin, P.J.T. Reardon, S.J.A. Moniz, J. Tang, Visible light-driven pure qater splitting by a nature-inspired organic semiconductor-based system, Journal of the American Chemical Society, 136 (2014) 12568-12571.
[18] H. Kato, M. Hori, R. Konta, Y. Shimodaira, A. Kudo, Construction of Z-scheme type heterogeneous photocatalysis systems for water splitting into $H_2$ and $O_2$ under visible light irradiation, Chemistry Letters, 33 (2004) 1348-1349.
[19] H. Kato, Y. Sasaki, N. Shirakura, A. Kudo, Synthesis of highly active rhodium-doped $SrTiO_3$ powders in Z-scheme systems for visible-light-driven photocatalytic overall water splitting, Journal of Materials Chemistry A, 1 (2013) 12327-12333.
[20] H. Fujito, H. Kunioku, D. Kato, H. Suzuki, M. Higashi, H. Kageyama, R. Abe, Layered perovskite oxychloride $Bi_4NbO_8Cl$: a stable visible light responsive photocatalyst for water splitting, Journal of the American Chemical Society, 138 (2016) 2082-2085.
[21] W. Wang, J. Chen, C. Li, W. Tian, Achieving solar overall water splitting with hybrid photosystems of photosystem II and artificial photocatalysts, Nature Communications, 5 (2014) 4647.
[22] Y. Sasaki, H. Kato, A. Kudo, $[Co(bpy)_3]^{3+/2+}$ and $[Co(phen)_3]^{3+/2+}$ Electron mediators for overall water splitting under sunlight irradiation using Z-scheme photocatalyst system, Journal

of the American Chemical Society, 135 (2013) 5441-5449.
[23] T. Kato, Y. Hakari, S. Ikeda, Q. Jia, A. Iwase, A. Kudo, Utilization of metal sulfide material of $(CuGa)_{1-x}Zn_{2x}S_2$ solid solution with visible light response in photocatalytic and photoelectrochemical solar water splitting systems, The Journal of Physical Chemistry Letters, 6 (2015) 1042-1047.
[24] K. Tsuji, O. Tomita, M. Higashi, R. Abe, Manganese-substituted polyoxometalate as an effective shuttle redox mediator in Z-scheme water splitting under visible light, ChemSusChem, 9 (2016) 2201-2208.
[25] Y. Miseki, S. Fujiyoshi, T. Gunji, K. Sayama, Photocatalytic Z-scheme water splitting for independent $H_2/O_2$ production via a stepwise operation employing a vanadate redox mediator under visible light, The Journal of Physical Chemistry C, 121 (2017) 9691-9697.